CrossMark

Motional Induction by Tsunamis and Ocean Tides: 10 Years of Progress

Takuto Minami[1]

Abstract Motional induction is the process by which the motion of conductive seawater in the ambient geomagnetic main field generates electromagnetic (EM) variations, which are observable on land, at the seafloor, and sometimes at satellite altitudes. Recent years have seen notable progress in our understanding of motional induction associated with tsunamis and with ocean tides. New studies of tsunami motional induction were triggered by the 2004 Sumatra earthquake tsunami and further promoted by subsequent events, such as the 2010 Chile earthquake and the 2011 Tohoku earthquake. These events yielded observations of tsunami-generated EM variations from land and seafloor stations. Studies of magnetic fields generated by ocean tides attracted interest when the Swarm satellite constellation enabled researchers to monitor tide-generated magnetic variations from low Earth orbit. Both avenues of research benefited from the advent of sophisticated seafloor instruments, by which we may exploit motional induction for novel applications. For example, seafloor EM measurements can serve as detectors of vector properties of tsunamis, and seafloor EM data related to ocean tides have proved useful for sounding Earth's deep interior. This paper reviews and discusses the progress made in motional induction studies associated with tsunamis and ocean tides during the last decade.

✉ Takuto Minami
    tminami@eri.u-tokyo.ac.jp

[1] Earthquake Research Institute, The University of Tokyo, 1-1-1 Yayoi, Bunkyo-ku, Tokyo 113-0032, Japan

🙲 Springer

1 Introduction

Conductive seawater moving in the ambient magnetic field generates electromotive forces (emfs) that result in electromagnetic (EM) field variations. This phenomenon, called motional induction, has interested physicists since the speculations of Faraday (1832). Studies in this field were stimulated by the advent of new instruments, including towed electrodes, submarine cables, seafloor EM sensors, and satellite-borne magnetometers. As these instruments provided new exciting data related to motional induction, especially since the 1940s, researchers have been developing new theories and numerical simulation methods to explain or predict EM phenomena.

Motional induction studies related to two phenomena, tsunamis and ocean tides, have made remarkable progress during the last decade. The reasons for this progress are different in the two cases, although the increment of new magnetic data from seafloor magnetometers played important roles in both. Tsunami-related motional induction studies followed the occurrence of several large tsunamigenic earthquakes since 2000 that yielded abundant observations of tsunami-related EM variations from land-based and seafloor instruments. As for ocean tides, the Swarm satellite constellation has opened the possibility of remotely monitoring ocean parameters by extracting tidally induced magnetic fields from satellite magnetic data (Sabaka et al. 2016), while inversion of the Earth's conductivity structure from tidal EM signals became feasible (Grayver et al. 2016).

In this paper, I focus on the most recent decade of advances in motional induction studies related to tsunamis and ocean tides. For this purpose, a brief review of older work on motional induction is helpful, because the theoretical underpinnings of this work, going back in intermittent stages to Faraday (1832), are still relevant for current discussions, and the classic papers are still worth reading today.

This paper is structured as follows: Sect. 2 outlines the progress of motional induction studies from Faraday's speculation to the 2000s. Section 3 reviews recent studies on tsunami-generated EM fields, and research on tide-generated EM fields is reviewed in Sect. 4. Section 5 summarizes the progress made during the last 10 years.

Whereas this paper mainly reviews recent progress focusing on tsunamis and ocean tides, many other reviews that cover a broader range of motional induction studies also provide useful background. Longuet-Higgins (1949) described the history of motional induction from Faraday's speculation to the 1940s. Filloux (1987) provided a comprehensive treatment of previous oceanic EM studies, including motional induction. Palshin (1996) reviewed the oceanic EM studies in the 1990s, including motional induction. Kuvshinov (2008) described studies on motional induction due to ocean circulation, ocean tides, and tsunamis in terms of global induction. Szuts (2012) comprehensively reviewed motional induction studies from the perspective of indirect ocean velocity measurement.

2 History of Motional Induction Studies

2.1 From Faraday to the 1950s

Faraday (1832) was the first to speculate that ocean flow in the geomagnetic field generates electric currents in the ocean. In an attempt to detect the electric potential due to the ocean tidal flow, he suspended copper plates from the parapet of the Waterloo bridge into the Thames River, but could not detect any signals greater than the noise level. It took almost

half a century until Adams (1881) first reported observations of tide-generated electric potential, although Wollaston had succeeded in measuring the electric potential with a lunar period in 1851 (Wollaston 1881). Both Adams and Wollaston used telegraph cables that were earthed in or near the ocean. This delay in confirming Faraday's insight is attributed to deficiencies in instrumentation and in understanding of the effects of a conductive seafloor (Young et al. 1920).

In the early 1900s, Young et al. (1920) first measured tide-generated electric potential variations with moored and towed electrodes. They found that the variations in electric potential with the semidiurnal ocean tide could not be in phase with the water velocity of the local tide, but instead were in phase with a stronger tidal stream in a remote position. This finding supported their idea that a conductive seafloor enables strong emfs to form large-scale electric circuits that control electric potential variations in remote areas where tidal streams are weak. This initial century of research is detailed by Longuet-Higgins (1949) and Filloux (1973).

In the 1930s and 1940s, several authors reported semidiurnal lunar variations of the geoelectric current at land-based observatories far from coastlines. For example, Egedal (1937) found lunar semidiurnal variations in north–south geoelectric potential data observed at Ebro, Spain, ~ 70 km from the coast, while Rooney (1938) determined similar periodic variations in electric potential data observed ~ 200 km inland at Tucson, USA, and ~ 150 km inland at Huancayo, Peru. Because the semidiurnal lunar variations were much smaller than the solar daily variations, Rooney adopted the method of Chapman and Miller (1940), in which hourly mean data are classified and stacked in terms of the lunar phase, to extract the lunar tidal variations. Although the true nature of these variations was obscure at that time (e.g., Egedal 1948), today we can conclude that the variations were generated by motional induction (e.g., Junge 1988).

In the 1940s and 1950s, many researchers got involved in theoretical studies of motional induction (e.g., Stommel 1948; Longuet-Higgins 1949; Longuet-Higgins et al. 1954; Malkus and Stern 1952). This was triggered by the development of the towed electrode technique (von Arx 1950). Because this technique exploits motionally induced electric potential to measure velocities in seawater, the new instrument was named the geomagnetic electrokinetograph (e.g., Filloux 1987). Longuet-Higgins et al. (1954) comprehensively investigated the relationship between seawater velocity and the resulting EM fields for specific cases of two-dimensional (2-D) stationary oceanic flows. The relationships they derived are useful for estimating water mass movements from electric potential data obtained by towed electrodes.

2.2 From the 1960s to the 1990s: Burgeoning Theory and Beginning of Seafloor Observations

After the study by Longuet-Higgins et al. (1954) came a variety of excellent theoretical works on motional induction, along with the advent of new seafloor EM instruments. Notably, the theoretical studies after 1960 addressed EM variations caused by time-varying oceanic flows with careful treatment of the self-induction effect, i.e., the effect of temporal variations of the magnetic field. The theories established in this period still underlie the interpretation of realistic motional induction phenomena today.

2.2.1 Short Waves and Swells

Motional induction due to surface gravity waves, which have short periods compared to other oceanic flows, were investigated with appropriate inclusion of the self-induction effect. Weaver (1965) presented an analytical solution for EM fields caused by short waves and swells assuming an infinitely deep ocean. The solution for short waves was demonstrated by measurements of EM fields using data from floating buoys (Maclure et al. 1964), seafloor magnetometers (Fraser 1966), and total field magnetometers above the sea surface (Ochadlick 1989). Cox et al. (1978) went on to explain the nonlinear mechanism by which wind-generated surface waves can cause magnetic variations at the deep seafloor.

2.2.2 Long Waves (Tsunamis)

Larsen (1971) derived analytical solutions of EM fields generated by long and intermediate waves (such as tsunamis), and investigated the self-induction and mutual induction effects on EM fields, by adopting a finite ocean depth and prescribing a layer of conducting sediment and a conductive mantle at a depth of a few tens to hundreds of kilometers. Larsen's solution, which is applicable to EM fields generated by tsunamis, was later reduced to a much simpler form by Tyler (2005). Chave (1983) derived an expression for tsunami-generated EM fields based on Green's functions. However, these theories for long waves were not confirmed by tsunami-generated EM fields until the twenty first century, mainly because of the transience of tsunami events. In the late 1990s, seafloor EM observatories for long-time operation were developed that incorporated fluxgate and Overhauser magnetometers (Toh et al. 1998). These led to the first report of tsunami-generated EM signals in the early 2010s (e.g., Toh et al. 2011).

2.2.3 Ocean Tides

The first seafloor in situ measurement of EM fields generated by ocean tides was achieved in the 1960s, benefitting from the development of seafloor EM sensors. Using the torsion fiber magnetometer (Filloux 1967), Larsen and Cox (1966) found that seafloor EM variations 600 km off the California coast with M_2 tidal periodicity (12.4206 h) were predominantly caused by motional induction. In the 1970s, fluxgate magnetometers (e.g., White 1979) were incorporated into seafloor instruments and are in common use today (e.g., Toh et al. 2006; Kasaya and Goto 2009). Refer to Filloux (1987) and Constable (2013) for more detailed description of developments of seafloor instruments in the late 1900s. As mentioned by Constable (2013), along with the advent of seafloor EM instruments, seafloor magnetotelluric (MT) surveys started in the 1960s. Since that time, motional induction phenomena also have been treated as sources of noise in seafloor MT studies (e.g., Cox 1980).

During this period, the seafloor EM instruments as well as conventional land-based observations promoted further understanding of tide-generated EM fields. Larsen (1968) was first to note the importance of self-induction on the tide-generated magnetic field in the open ocean and conducted numerical simulations adopting the thin-shell approximation (Price 1949). In a theoretical advance, Chave (1983) recognized the importance of the galvanic connection between the ocean layer and the conductive seafloor in tide-generated EM fields by adopting a representation based on Green's functions and by treating the

toroidal magnetic (TM) mode and the poloidal magnetic (PM) mode separately. It was also found that land-based EM data with M_2 periodicity were influenced by motional induction due to ocean tides (e.g., Larsen 1968; Harvey et al. 1977; Junge 1988).

2.2.4 Large-Scale Low-Frequency Oceanic Flows

In the field of large-scale low-frequency barotropic oceanic flow, Sanford (1971) extended the 2-D theory of Longuet-Higgins et al. (1954) to three-dimensional (3-D) time- and space-varying oceanic flows. By restricting the phase velocity of oceanic flow to less than ∼10 m/s, where the effect of self-induction is negligible, Sanford (1971) derived relationships between low-frequency large-scale barotropic flows and the EM fields they generate. He pointed out the importance of conductivity-weighted, vertically averaged velocity for the generation of both local and large-scale electric currents.

In the 1980s and 1990s, seafloor electric fields and potentials were utilized to estimate ocean mass transport. Based on the theoretical work of Sanford (1971), Larsen and Sanford (1985) and Larsen (1992) inferred the mass transport in the Florida Strait from the electric voltage difference measured by submarine cables. Segawa and Toh (1992) also used a submarine cable to investigate the transport of the Kuroshio at the Nankai Trough. Chave and Luther (1990) and Luther et al. (1991) showed that measurements of the horizontal electric field at the seafloor can serve as an efficient metric of barotropic flow in the central North Pacific, in the Barotropic, EM and Pressure Experiment (BEMPEX) project (Luther et al. 1987).

2.2.5 Development of Horizontal Ocean Velocity Profilers

In the 1970s, motionally induced electric fields within the ocean layer began to be used for detailed studies of ocean flow. Sanford et al. (1978, 1982) developed the recoverable/expendable relative velocity profiler, which measures a vertical profile of relative horizontal ocean velocity while freely falling to the seafloor. Sanford et al. (1985) developed the "absolute" velocity profiler, which uses an acoustic Doppler instrument to measure the velocity of the profiler with respect to the seafloor. These velocity profilers were later incorporated in multifunctional floats like the EM Autonomous Profiling Explorer (EM-APEX; Sanford et al. 2005) and remain in common use today (e.g., Sanford et al. 2007, 2011).

2.2.6 Studies of Baroclinic Waves

This period saw motional induction studies extended to baroclinic waves, i.e., oceanic flows that have vertical shear in the horizontal components. Podney (1975), Petersen and Poehls (1982), and Chave (1984) theoretically investigated the magnetic fields generated by baroclinic internal waves, and Podney and Sager (1979) succeeded in identifying the magnetic gradients originating from internal waves. This line of research later led to the first report of magnetic variations generated by passage of an ocean eddy (Lilley et al. 1993) and the derivation by Tyler and Mysak (1995) of analytical solutions applicable to vertically and horizontally sheared plane-parallel flows.

2.3 The 1990s and 2000s: Advent of Global Numerical Simulations and Satellite Observations

Satellite-borne magnetometers and the development of numerical simulation techniques were the most notable innovations of the 1990s and 2000s, while the velocity profilers utilizing motional induction came into common use in oceanography. Numerical simulations of motional induction phenomena started in the 1990s. Most of the simulation studies mentioned here are described in detail by Kuvshinov (2008) in a comprehensive review of 3-D global simulation studies, including those for EM fields of oceanic origin.

2.3.1 Ocean Circulation Simulations

The 1990s saw the first useful simulations related to steady ocean circulation. Stephenson and Bryan (1992), Tyler et al. (1997), and Vivier et al. (2004) applied the thin-shell approximation of Price (1949) to calculate magnetic fields generated by steady ocean circulation, regarding the model layers above and beneath the ocean layer as insulators. Notably, Vivier et al. (2004) found a strong correlation (>95%) between the Antarctic Circulation Current (ACC) transport and the calculated magnetic field in some regions. Two other noteworthy studies conducted full 3-D simulations that included realistic conductivity beneath the seafloor: Flosadóttir et al. (1997) adopted the 3-D finite difference method (Smith 1996a, b) and Manoj et al. (2006) employed the integral equation (IE) method (Kuvshinov et al. 2002).

The simulation techniques for ocean circulation developed in the 1990s and 2000s are still used today. After the launch of the Swarm satellites, determining the feasibility for remotely monitoring ocean circulation and related ocean parameters via satellite magnetic observations became of interest. Along with the technique of Vivier et al. (2004), Irrgang et al. (2016a, b) investigated the uncertainty of the magnetic variations arising from errors in the source input, i.e., seawater velocity, related parameters, e.g., seawater conductivity, and the simulation model itself.

2.3.2 Ocean Tides

The advent of satellite magnetic observations promoted studies of motional induction by ocean tides in the early 2000s, while conventional observations from submarine cables were still common (e.g., Nolasco et al. 2006). Tyler et al. (2003) showed that magnetic variations generated by the M_2 tidal component can be detected at the altitude of the CHAMP (CHAllenging Minisatellite Payload) satellite, by comparing satellite observations with their global simulation results. Later, Maus and Kuvshinov (2004) and Kuvshinov and Olsen (2005), and Kuvshinov et al. (2006) conducted 3-D global simulations that revealed features arising from motional induction due to ocean tides. These studies are discussed in Sect. 4.3.

2.3.3 Tsunamis

Thomson et al. (1995) were the first to detect tsunami-generated electric potentials in submarine cables, attributing an $\sim$30-min echo in the cable electric potential following the 1992 Cape Mendocino earthquake to tsunami motional induction. A long pause in this line of research since the papers of Larsen (1971) and Chave (1983) ended after the devastating

2004 Sumatra earthquake and tsunami, and studies of tsunami motional induction resumed in earnest in the 2000s. The most important contributions during this period were made by Tyler (2005) and by Manoj et al. (2010).

Tyler (2005) derived a simple relationship between the tsunami sea surface displacement and the generated magnetic field. Tyler also showed that tsunami-generated magnetic fields were unlikely to be detected at typical satellite altitudes of ~ 400 km, because the horizontal scale of tsunamis ($\sim 10^2$ km) is much smaller than those of ocean tides ($\sim 10^3$ km).

Manoj et al. (2010) investigated whether submarine cables in the Indian Ocean could detect the electric field generated by the 2004 Sumatra tsunami by applying their global induction technique to tsunami-generated magnetic fields. They found that observable voltages as great as ~ 0.5 V were induced between the ends of submarine cables. While Manoj et al. (2010) cited advantages to submarine cables owing to their widespread presence and the small expense of making observations, later studies were to show that in situ seafloor EM field observations can provide more information on tsunami propagation than submarine cables (e.g., Toh et al. 2011).

2.3.4 Application of a Variety of EM Instruments

In the 2000s, motional induction studies employed a wide range of EM instruments in addition to satellite-borne magnetometers and sophisticated seafloor instruments. Lilley et al. (2004) used floating magnetometers to detect the magnetic field generated by ocean swells. Sanford et al. (2007) airdropped a profiling float equipped with the EM-APEX velocity profiler (Sanford et al. 2005) into the upper ocean ahead of Hurricane Frances in 2004 and succeeded in obtaining data on the ocean response to a category 4 hurricane. The profiler data revealed that the passage of the hurricane generated inertially rotating currents of appreciable velocity (>1 m/s) in the upper 120 m of the water column.

The improvement in velocity profilers exploiting motional induction still continues today. Terker et al. (2013) developed a new free fall absolute profiler that measures the position by GPS satellites at the beginning and end of round trip to the seafloor, during which a compass coil is used to determine the direction of the electrode arm and the rotation rate of the instrument. On the other hand, the EM-APEX velocity profiler plays more important roles in today's oceanography. They were introduced to large-scale projects to investigate features of global ocean circulation, e.g., Kuroshio (Andres et al. 2015)

3 Motional Induction by Tsunamis

Starting with the 2004 Sumatra event, magnetic observations at the time of great earthquakes have led to dramatic progress in our understanding of motional induction related to tsunamis. This section reviews recent observation reports in Sect. 3.1, theoretical advances in Sect. 3.2, developments in numerical techniques in Sect. 3.3, and possible applications of tsunami motional induction in Sect. 3.4.

3.1 EM Data Due to Tsunami Motional Induction

Many reports of tsunami-generated EM variations, observed both on land and at the seafloor, have appeared during the last decade. These studies succeeded not only because several large tsunami earthquakes occurred during a period of relatively quiet solar activity (e.g., the 2006/2007 Kuril, 2010 Chile, and 2011 Tohoku events), but also because many sophisticated ocean bottom instruments were collecting data, especially in the Pacific Ocean, during the tsunami events.

3.1.1 The 2006 and 2007 Kuril Earthquake Tsunamis

The first report of evident tsunami-generated EM fields was that of Toh et al. (2011), who detected EM variations due to the 2006 and 2007 Kuril earthquake tsunamis with the SeaFloor ElectroMagnetic Station (SFEMS) system (Toh et al. 1998, 2006). The EM components and tilt observations at the time of the 2006 Kuril earthquake, shown in the left column of Fig. 1, display clear responses of EM components to the arrival of the tsunami, but no response to the arrival of the seismic waves. Toh et al. (2011) concluded that a seafloor EM sensor at a single site can monitor both the tsunami propagation direction and
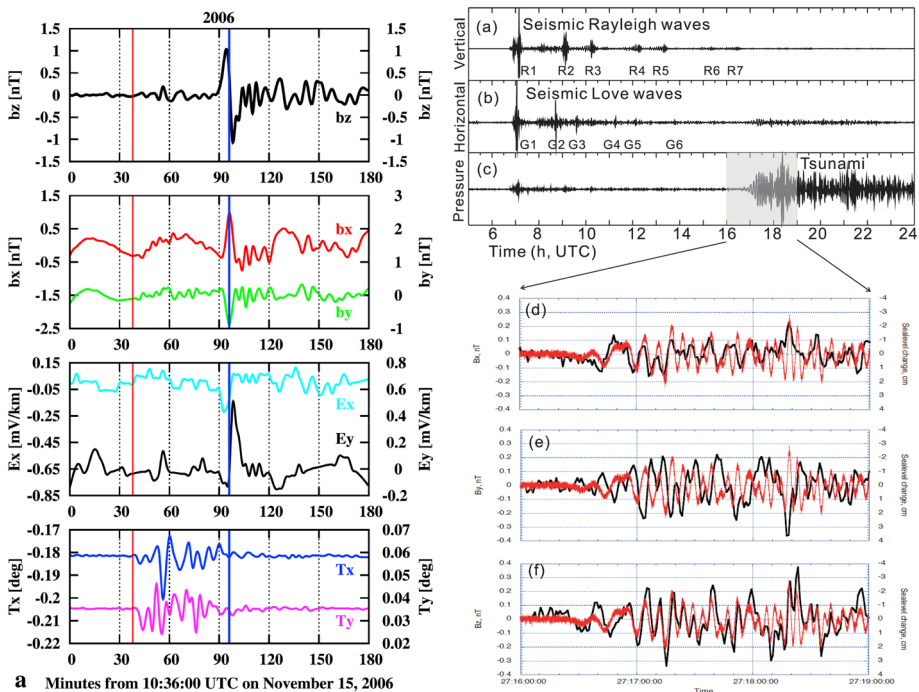
Fig. 1 Reports of tsunami-generated EM variations. *Left panel* shows time series of tsunami EM components and tilt variation at the time of the 2006 Kuril earthquake tsunami (Toh et al. 2011). *Red* and *blue vertical lines* denote the earthquake occurrence and the estimated tsunami arrival time at the seafloor site, respectively. *Right panel* shows the three magnetic components (*black lines*) and pressure data (*red lines*) at the time of the 2011 Chile earthquake tsunami (Suetsugu et al. 2012). Subscripts x, y, and z indicate the northward, eastward, and downward components

the tsunami wave height. This idea led soon after to the development of an innovative seafloor sensor for use in rapid tsunami determinations (see Sect. 3.4.3).

3.1.2 The 2009 Samoa Earthquake Tsunami

Schnepf et al. (2016) recently found clear magnetic variations coinciding with the arrival of the tsunami from the 2009 Samoa earthquake in seafloor magnetic data obtained in French Polynesia during the Tomographic Investigation by seafloor ARray Experiment for the Society hotspot (TIARES) project (e.g., Suetsugu et al. 2012). TIARES data had previously been examined in connection with the 2010 Chile earthquake tsunami, as described in the next subsection.

Schnepf et al. (2016) detected the tsunami magnetic signals with a new cross-wavelet analysis method to highlight tsunami magnetic signals, which reduced red noise by utilizing the horizontal magnetic fields at a reference point. They applied their method to magnetic data obtained during the 2007 Kuril, 2010 Chile, and 2011 Tohoku tsunamis as well as the Samoa event. Their method successfully extracted time–frequency characteristics of tsunami magnetic signals. At present, the only drawback of their method is an inability to reproduce the time series after noise reduction by the cross-wavelet analysis, which leads to loss of the phase information in the original time series.

3.1.3 The 2010 Chile Earthquake Tsunami

Manoj et al. (2011) first reported variations in land-based magnetic data generated by tsunamis, using observations from Easter Island at the time of the 2010 Chile earthquake tsunami. Although land-based observations are often severely contaminated by variations originating from the magnetosphere, exceptionally quiet magnetic conditions allowed variations of ~ 1 nT to be recorded at that time. Wang et al. (2015) verified that the Chile tsunami was the cause of these magnetic variations by applying the analytical solution of Tyler (2005) to a simulation of the tsunami.

Suetsugu et al. (2012) and Sugioka et al. (2014) first reported concurrent seafloor observations of water pressure and magnetic signals made at the time of the 2010 Chile earthquake tsunami during the TIARES project (Suetsugu et al. 2012). The right panel of Fig. 1 shows the clear correlation between perturbations in the magnetic field and seafloor pressure, both of which were proportional to the tsunami sea surface displacement. This strong correlation confirmed Tyler's (2005) prediction that the vertical component of the magnetic field would respond in phase with the tsunami sea surface displacement in the deep ocean.

After the time of the 2010 Chile event, the wavelet transform data-processing technique was first introduced for the analysis of tsunami-generated magnetic variations by Klausner et al. (2014). By applying the gapped wavelet analysis method (Frick et al. 1997), which has the advantage of utilizing both the oscillatory and envelope waveforms, they succeeded in highlighting magnetic variations corresponding to the tsunami in magnetic data from Easter Island and the Papeete station (Tahiti) during the 2010 Chile tsunami event. This highlighting technique can reduce the work involved in conventional visual inspection of the original time series.

3.1.4 The 2011 Tohoku Earthquake Tsunami

The 2011 Tohoku earthquake tsunami yielded EM data from both land-based and seafloor observations. Using land-based observations, Utada et al. (2011) described magnetic

variations originating from the tsunami that included signals due to ionospheric distur-
bances caused by tsunami-generated acoustic-gravity waves (AGWs) as well as motional
induction from the tsunami. Tatehata et al. (2015) analyzed the magnetic variations
observed at the Chichijima Island station (CBI) by a numerical simulation based on the
formula of Tyler (2005).

Using seafloor observations, Minami and Toh (2013) reported tsunami-related magnetic
variations as large as approximately 3 nT in observations from the northwest Pacific
seafloor. Using seafloor magnetic variation data obtained just to the east of the Japan
Trough, Ichihara et al. (2013) made the first attempt to constrain the tsunami source region
from magnetic data (see Sect. 3.4.2 for details). Zhang et al. (2014a, b) reported seafloor
EM data from the north Pacific, where an array of seafloor instruments was installed by the
Normal Oceanic Mantle project (Kawakatsu et al. 2013), and were able to accurately
determine the tsunami propagation direction in that area. Because high-frequency external
variations cannot reach the seafloor, most of the EM signals from the seafloor were clear
and useful for inferring the dynamic properties of the tsunami propagation. Most of the
papers mentioned here except Ichihara et al. (2013) conducted numerical EM simulations
to explain the observed tsunami-generated seafloor magnetic variations. The details of
these simulations are reviewed in Sect. 3.3.

3.1.5 Magnetic Variations Due to Tsunami-Generated Acoustic-Gravity Waves

During tsunami events, magnetic variations are caused not only by tsunami motional
induction but also by tsunami–atmosphere–ionosphere (TAI) coupling (e.g., Tsugawa et al.
2011; Utada et al. 2011; Kherani et al. 2016). AGWs excited by large tsunamis can reach
the ionosphere and cause ionospheric dynamo currents and secondary magnetic fields that
are observable at ground magnetic observatories.

Klausner et al. (2016) concluded that during the 2011 Tohoku tsunami, the downward
component of the magnetic variations (B_z) preceding the tsunami arrival by 10–40 min,
such as in land-based observations of B_z at CBI, originated not from motional induction but
from the ionospheric current excited by tsunami-generated AGWs. In contrast, Zhang et al.
(2014b) and Tatehata et al. (2015) concluded from numerical simulations that these
variations were generated by motional induction. Figure 2 compares these three analyses.

3.1.6 Identification of Magnetic Signals Prior to Tsunami Arrival

An unsolved problem in EM variations due to tsunamis is that there is no obvious criterion
to judge whether a magnetic field variation is due to motional induction or the ionospheric
current excited by tsunami-generated AGWs. In the case of magnetic data from CBI during
the 2011 Tohoku tsunami, it is safe to conclude that the B_z variation $\sim$ 10 min prior to the
simulated tsunami arrival was generated by motional induction, because the simulations of
motional induction presented by Tatehata et al. (2015) and Zhang et al. (2014b) both
agreed well with the observations at CBI, especially in their phase, as shown in Fig. 2.
However, it might be difficult to rule out TAI coupling if we were limited to the infor-
mation presented by Klausner et al. (2016).

One possible reason that B_z variations precede the tsunami arrival at CBI is that, in
theory, B_z precedes tsunami sea surface displacement by a tsunami phase angle of
approximately $\pi/4$ in very shallow oceans (Tyler 2005; Minami et al. 2015; see Sect. 2.2
and Fig. 3), which would be the case for island observatories near the coast, such as CBI.
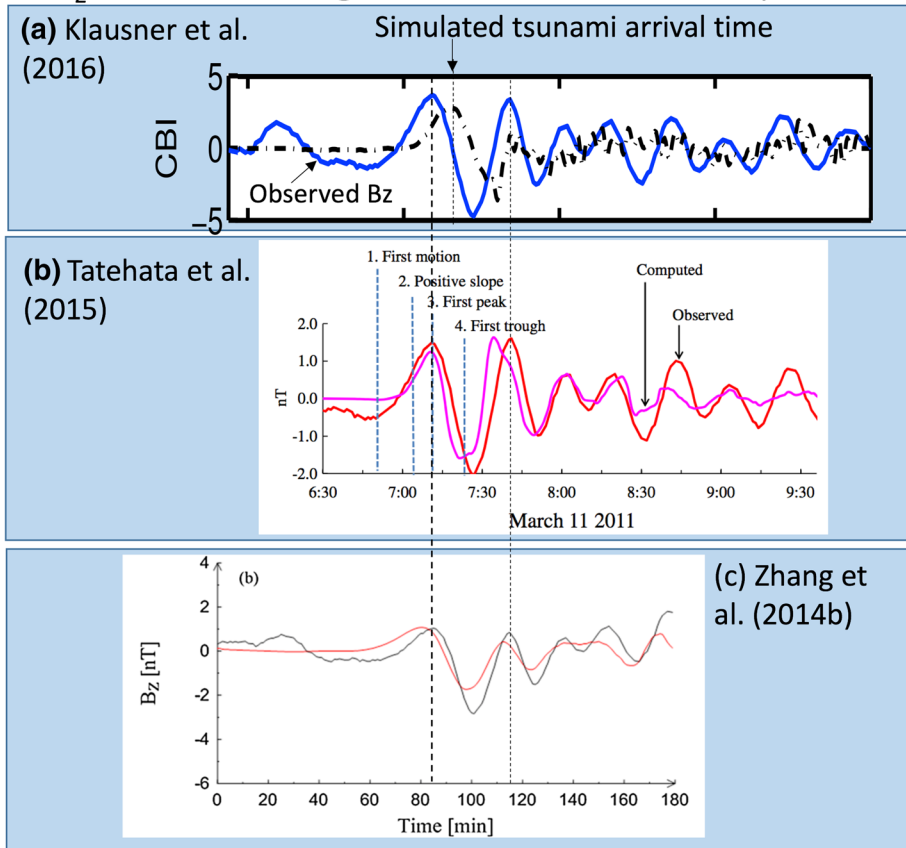This theoretical consideration, along with the distance between the magnetic observatory

Fig. 2 Analyses of B_z (downward) observed at CBI during the 2011 Tohoku tsunami. **a** Klausner et al. (2016) presented the B_z observations (*blue line*) and simulated tsunami wave heights (*dashed line*) from a model by Sladen and Hébert (2008) at a point 11 km from the CBI magnetic observatory. The B_z variation ∼10 min prior to the tsunami height peak was attributed to the effects of TAI coupling. **b** Tatehata et al. (2015) presented B_z observations (*red line*) and B_z simulated by the modified Tyler's method (*pink line*). **c** Zhang et al. (2014b) presented the B_z observations (*black*) and B_z simulated by their 3-D motional induction code. The slight differences among the B_z observations should arise from differences in the adopted data-processing methods

and the tide gauge or the simulated tsunami arrival location, could account for the ∼10 min difference between the B_z variation and the tsunami arrival at CBI. Identifying premonitory magnetic variations would require numerical simulations of tsunami motional induction and/or of tsunami-generated AGWs, but simulation studies of TAI coupling that can directly calculate magnetic fields at the ground do not yet exist. For this purpose, induction effects due to the conductivity of the solid Earth should be included in the modeling, as well as the TAI coupling itself.

A similar identification problem has been posed by Klausner et al. (2014), who found in their study of the Chile tsunami that magnetic variations with the tsunami period occurred at the Papeete station approximately 2 h before the tsunami arrived there. They suggested that a large-scale electrical circuit in the ocean due to motional induction could have
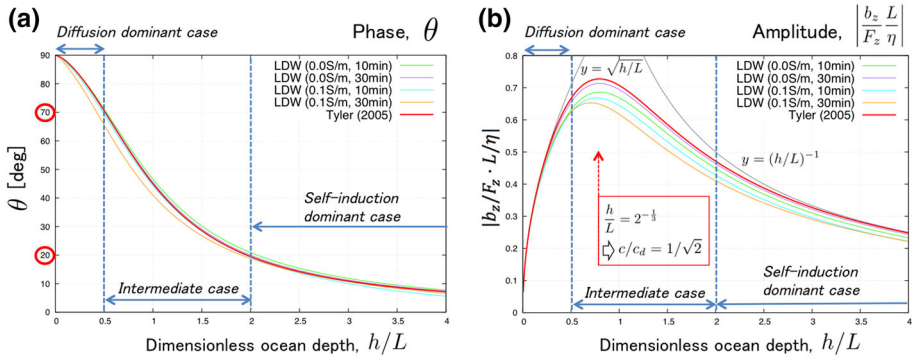
Fig. 3 *Left* Phase of the vertical component of the tsunami magnetic field (b_z) relative to the tsunami sea surface displacement (θ), where $\theta = 90°$ means the $\pi/4$ phase lead of b_z to η. *Right* Normalized amplitude, $|b_z L/F_z \eta|$, with respect to normalized ocean depth, h/L. In both panels, the lines titled LDW(σ, T) are analytical solutions of Minami et al. (2015), where LDW stands for the linear dispersive wave expression given in Eq. (5), σ is the half-space conductivity beneath the seafloor, and T is the period of the tsunami. The *red line* is an analytical solution from Tyler (2005). Note that $L = \left(2K/\sqrt{g}\right)^{2/3} \sim 2.7$ km

caused these magnetic signals. There is no obvious way to rule out either motional induction or AGWs, which leaves this case an outstanding problem for numerical modelers.

3.2 Theory of EM Fields Caused by Tsunami Motional Induction

In theoretical studies of tsunami motional induction, the most commonly adopted governing equation is the magnetic induction equation,

$$\frac{\partial \mathbf{B}}{\partial t} = \nabla \times (\mathbf{v} \times \mathbf{B}) - \nabla \times (K\nabla \times \mathbf{B}), \tag{1}$$

where $K = (\mu\sigma)^{-1}$ is the magnetic diffusion coefficient, μ is the magnetic permeability, σ is the magnetic conductivity, $\mathbf{B}$ is the magnetic field, and $\mathbf{v}$ is the seawater velocity. If we decompose the magnetic field into the ambient geomagnetic main field, $\mathbf{F}$, and the tsunami-generated magnetic field, $\mathbf{b}$, Eq. (1) is reduced to

$$\frac{\partial \mathbf{b}}{\partial t} = \nabla \times (\mathbf{v} \times \mathbf{F}) - \nabla \times (K\nabla \times \mathbf{b}), \tag{2}$$

where $|\mathbf{F}| \gg |\mathbf{b}|$, $|\nabla \times \mathbf{F}| \ll 1$, and $\partial \mathbf{F}/\partial t = 0$ are assumed. These assumptions are acceptable when we assume $\mathbf{v}$ as the seawater velocity of a tsunami. Almost all theoretical studies of tsunami motional induction begin with Eq. (2) with the exception of Chave (1983), who adopted the TM/PM modal representation. Many theoretical works on tsunami motional induction assume a one-dimensional (1-D) layered Earth with a homogeneous conductivity in each layer, including an ocean layer with a constant depth. These assumptions lead to the conductivity being represented as $\sigma = \sigma(z)$, where z is the vertical position, downward positive, and $z = 0$ at the sea surface. By further assuming that $\nabla \cdot \mathbf{v} = 0$, $\nabla \cdot \mathbf{F} = 0$, and $|(\mathbf{v} \cdot \nabla)\mathbf{F}| \ll |(\mathbf{F} \cdot \nabla)\mathbf{v}|$, this 1-D configuration, in which the horizontal gradient of conductivity equals 0, enables us to derive a simple equation in terms of the vertical component b_z from Eq. (2),

$$\frac{\partial b_z}{\partial t} = (\mathbf{F} \cdot \nabla)v_z + K\nabla^2 b_z. \tag{3}$$

Note that $\nabla \times (\mathbf{v} \times \mathbf{F}) = (\nabla \cdot \mathbf{F})\mathbf{v} - (\nabla \cdot \mathbf{v})\mathbf{F} + (\mathbf{F} \cdot \nabla)\mathbf{v} - (\mathbf{v} \cdot \nabla)\mathbf{F}$ is used. Eq. (3) is referred to as the PM mode equation (e.g., Chave 1983). Benefitting from $\nabla \cdot \mathbf{v} = 0$, the source term $(\mathbf{F} \cdot \nabla)v_z$ can be decoupled into two terms, $\boldsymbol{F}_H \cdot (\nabla_H v_z)$ and $-F_z(\nabla_H \cdot \mathbf{v}_H)$, where the subscription H denotes the horizontal vector component, which indicate contributions from couplings of the ocean flow with $\boldsymbol{F}_H$ and F_z, respectively. After solving Eq. (3), the other components of tsunami-generated EM fields can be calculated from $\nabla \cdot \mathbf{b} = 0$ and $\nabla \times \mathbf{e} = -\partial \mathbf{b}/\partial t$, where $\mathbf{e}$ is the tsunami-generated electric field.

As for the TM mode, Larsen (1971) showed that the TM mode is not excited by tsunami motional induction. When we consider a tsunami propagating in the y-direction, expressed as $\mathbf{v} = (v_x, v_y, v_z)$ with $v_x = 0$, a loop integral of the emf along an arbitrary closed circuit in the y, z plane, C_{yz} with the area of S_{yz}, vanishes as

$$\oint_{C_{yz}} (\mathbf{v} \times \mathbf{F}) \cdot ds = \iint_{S_{yz}} [\nabla \times (\mathbf{v} \times \mathbf{F})]_x dydz = \iint_{S_{yz}} (\mathbf{F} \cdot \nabla)v_x dydz = 0, \tag{4}$$

by Stokes' theorem. Eq. (4) shows that the emf shorts out along any circuits in the y,z plane so that no vertical electric field is induced by plane-wave tsunamis. As a result, there is no need to consider the TM mode for tsunami motional induction, thanks to the conditions of $\nabla \cdot \mathbf{v} = 0$, $\nabla \cdot \mathbf{F} = 0$, and $|(\mathbf{v} \cdot \nabla)\boldsymbol{F}| \ll |(\boldsymbol{F} \cdot \nabla)\mathbf{v}|$. This is not the case in tidal motional induction, because $|(\mathbf{v} \cdot \nabla)\boldsymbol{F}|$ cannot be ignored given the much longer wavelength of ocean tides and because v_x takes a nonzero value due to the Coriolis force during the time scale of ocean tides.

Thus, all existing analytical solutions for tsunami-generated EM fields involve only the PM mode and are derived by solving Eq. (3) with various assumptions. The simplest expression was presented by Tyler (2005), the most comprehensive expression was given by Larsen (1971) and Shimizu and Utada (2015), and several other expressions fall in between (Ichihara et al. 2013; Sugioka et al. 2014; Minami et al. 2015). The assumptions and characteristics of these solutions are summarized in Table 1.

Note that there are two kinds of tsunami seawater velocity models: the linear dispersive wave model,

Table 1 Characteristics of analytical solutions for tsunami-generated EM fields

Publication	Tsunami velocity model	Sub-seafloor type	Main field	Characteristics
Larsen (1971)	LDW	Three-layered Earth model	F_H and F_z	Investigates shallow and deep mantle models
Tyler (2005)	LLW	Half-space insulator	F_z	Independent of frequency
Ichihara et al. (2013) Sugioka et al. (2014)	LLW	Homogeneous half-space	F_z	Conductive homogeneous Earth model
Minami et al. (2015)	LDW	Homogeneous half-space	F_z	Considers conservation of dynamic energy
Shimizu and Utada (2015)	LDW	Arbitrary 1-D Earth	F_H and F_z	General form of Larsen (1971)

LDW linear dispersive wave (Eq. 5), *LLW* linear long wave (Eq. 6)

$$\mathbf{v} = \left(0, \omega \frac{\cosh(k(h-z))}{\sinh(kh)}\eta, i\omega \frac{\sinh(k(h-z))}{\sinh(kh)}\eta\right) \quad (0<z<h), \tag{5}$$

and the linear long wave model,

$$\mathbf{v} = \left(0, c\frac{\eta}{h}, i\omega \frac{h-z}{h}\eta\right) \quad (0<z<h), \tag{6}$$

where the tsunami propagation direction is set in the y-direction, and the sea surface displacement is expressed as $\eta \propto \exp(i(ky - \omega t))$ with wavelength k and angular frequency ω. The sea surface and seafloor are represented by $z = 0$ and $z = h$, respectively. Equation (6) is easily derived from Eq. (5) by considering wavelengths much greater than the ocean depth, such that $kh \to 0$.

Here I focus on the analytical solutions by Tyler (2005) and Minami et al. (2015). First, Tyler's expression is notable for its simple form, given by

$$\frac{b_z}{F_z} = \frac{c}{c + ic_{\mathrm{d}}}\frac{\eta}{h}, \quad z = 0 \text{ or } h, \tag{7}$$

where $c = \sqrt{gh}$ is the tsunami phase velocity and $c_{\mathrm{d}} = 2K/h$ is the lateral magnetic diffusion velocity. Tyler (2005) simplified the relationship derived by Larsen (1971) by adopting the linear long wave formulation of Eq. (6), an insulating layer beneath the seafloor, and the assumption that the skin depth of seawater is much longer than the ocean depth, $\sqrt{2K/\omega} \gg h$. These assumptions result in Eq. (7), where the conversion coefficient, $c/(c + ic_{\mathrm{d}})$, is independent of frequency. Equation (7) indicates that, in the deep ocean, b_z is in phase with η, as represented by $b_z/F_z \approx \eta/h$. This feature is clearly identified, for example, in the comparison between seafloor magnetic data and pressure data, as shown in the right column of Fig. 1. Another notable feature of Eq. (7) is that the effect of the conductive layer beneath the seafloor was neglected in the derivation, which is also validated by many other analytical studies. For example, Fig. 3 shows a comparison between Eq. (7) and the solutions derived by Minami et al. (2015), in which the horizontal axis is the regularized ocean depth, h/L, where $L = (2K/\sqrt{g})^{2/3} \sim 2.7$ km. The discrepancies between Tyler's solution and the other solutions are trivial, which demonstrates that the assumption adopted in Tyler (2005) is reasonable. Figure 3 also shows no significant differences in both phase and amplitude among the solutions derived by Minami et al. (2015), which implies that tsunami magnetic fields are not a viable tool to explore the conductivity beneath the seafloor. Shimizu and Utada (2015) recently investigated the feasibility of using tsunami EM signals to constrain sub-seafloor conductivity. Their work is discussed further in Sect. 3.4.1.

Figure 3 shows another interesting feature of the tsunami-generated magnetic field: its dependence on ocean depth. The relative phase of b_z to η, θ, differs monotonically from 90° to $\sim 10°$ as the ocean is deepened from 0 to ~ 10.8 km, while the regularized amplitude, $|b_z L/F_z \eta|$, has a peak at a depth of approximately $h/L = 2^{-1/3}$, or approximately 2.1 km. As pointed out by Minami et al. (2015), the diffusion term $K\nabla^2 b_z$ in Eq. (3) is much larger than the self-induction term $\partial b_z/\partial t$ in shallow oceans and much smaller than self-induction in deep oceans, which leads to the monotonic phase variability and amplitude peak at intermediate depths. Thus Fig. 3 implies that the signal-to-noise ratio of tsunami magnetic signals may be dominantly controlled by ocean depth. Minami et al. (2015) also showed that the peak of the regularized amplitude shifts toward shallower oceans when considering the conservation of the dynamical energy of a tsunami (i.e.,

$\sqrt{gh} \times (1/2)\rho g|\eta|^2 =$ const.) during its propagation. These features should be taken into account in designs of future tsunami observations.

All the features of tsunami EM signals mentioned here are useful in predicting tsunami-generated EM fields. However, difficulties arise when evaluating the effect of bathymetry, which requires numerical modeling with realistic bathymetry.

3.3 Numerical Simulations of Tsunami-Generated EM Fields

We can regard motional induction problems as analogs of controlled source electromagnetic problems in which the source electric current, j_s, is replaced by the product of the ocean conductivity and emf due to tsunamis, $\sigma(\mathbf{v} \times \mathbf{F})$. Thus, many existing EM modeling techniques can be applied to simulations of motionally induced EM fields with minor adjustments. Recently, a wide variety of numerical methods have appeared for simulations of tsunami-generated EM variations.

Manoj et al. (2010) were probably the first to simulate tsunami-generated EM fields. They applied the global IE technique of Kuvshinov et al. (2002) to 3-D global simulations of tsunami EM variations, to investigate whether submarine cables in the Indian Ocean could detect the voltage difference caused by the 2004 Sumatra earthquake tsunami. This study was partly motivated by Thomson et al. (1995), which documented voltage variations across an undersea cable that appeared to be related to the 1992 Cape Mendocino earthquake tsunami. Manoj et al. (2010) showed that the Sumatra tsunami produced measurable electric voltages of the order of ±500 mV (also see Fujii and Chave 1999) across the submarine cables in the Indian Ocean. One drawback of their simulation was the coarse horizontal resolution of $1° \times 1°$, which did not yield results that could be compared with in situ EM observations from the seafloor.

Many subsequent reports of tsunami EM variations in the early 2010s required accurate numerical simulations that could reproduce variations in comparable detail to in situ measured data. Utada et al. (2011) were the first to simulate the magnetic field generated by the 2011 Tohoku earthquake tsunami, although their reliance on the Biot–Savart law, neglecting the self-induction effect ($\partial \mathbf{b}/\partial t$) in Eq. (2), limited the simulation's accuracy.

Minami and Toh (2013) developed a 2-D time-domain simulation code to reproduce magnetic variations in the northwest Pacific generated by the 2011 Tohoku tsunami, adopting the finite element method for spatial discretization and the Crank–Nicolson method for temporal discretization. They calculated the tsunami oceanic flow from the fault slip model of Maeda et al. (2011) and used the resulting velocity field to calculate the tsunami-generated magnetic fields. Figure 4 shows that they successfully reproduced both the sea surface displacement data from DART observatories (e.g., Bernard and Meinig 2011) and the tsunami magnetic variations. Note in Fig. 4 that the initial rise in the horizontal component b_y (in the tsunami propagation direction) preceded the arrival of the tsunami peak by approximately 5 min at seafloor EM observatory NWP, while the peak of the vertical component was almost in phase with the sea surface displacement, as expected from Eq. (7).

Zhang et al. (2014b) adopted the modified iterative dissipative method (e.g., Singer 1995) based on the IE technique to successfully perform 3-D numerical simulations of seafloor EM variations from the 2011 Tohoku tsunami. They prescribed a realistic 3-D conductivity structure beneath the seafloor based on the 1-D conductivity structure in the Pacific Ocean reported by Baba et al. (2010). One drawback of their simulation is that the calculation was conducted in the frequency domain, which requires source seawater
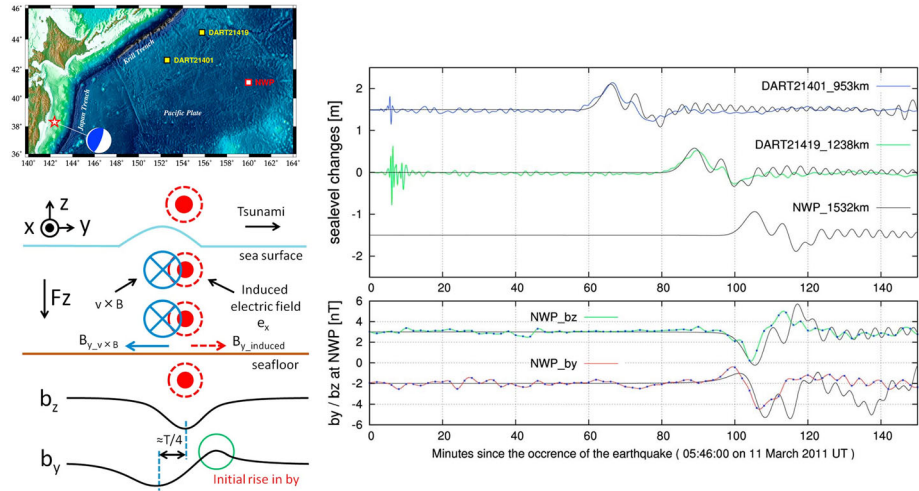
Fig. 4 Two-dimensional tsunami magnetic simulations for the 2011 Tohoku earthquake tsunami by Minami and Toh (2013). The map shows locations of the epicenter (*star*), DART observation sites (*yellow rectangles*), and seafloor EM observatory (*red rectangle*). The *right panel* shows comparisons of sea surface elevation (*top*) and of magnetic fields (*bottom*), where *colored lines* indicate observed data and *black lines* are simulation results. Note in Minami and Toh (2013) that the z axis is upward positive, opposite to our definition, and the y axis is in the tsunami propagation direction. The *left lower panel* shows the mechanism by which tsunami propagation generates the initial rise in b_y

velocities in the frequency domain although the tsunami simulations were performed in the time domain (Maeda et al. 2011). Frequency-domain simulations that require a Fourier transform against seawater velocity in the time domain is computationally expensive compared to time-domain simulations, such as that of Minami and Toh (2013). Figure 5 summarizes the results of Zhang et al. (2014b). Although the peak times at CBI and at seafloor site NM04 were well explained by the 3-D simulations, the discrepancy between simulated and observed time series at NM04 became large after the first peak. These results can be attributed to the elimination of dispersive properties in the linear long wave approximation (Zhang et al. 2014b). On the other hand, at the land magnetic observatory ESA, the discrepancy between the simulation and observations was very large. As the authors mentioned, the variation in the observed field starting about 10 min after the origin time was probably caused by an ionospheric disturbance (e.g., Tsugawa et al. 2011) and therefore should not be compared with the simulation. This discrepancy remains to be explained by future studies.

Tatehata et al. (2015) adopted another approach in their simulation of tsunami-generated EM variations, improving the Biot–Savart simulation method of Utada et al. (2011) by applying the analytical solution of Tyler (2005). They assumed at every grid point of their simulation space that tsunamis can be approximated by plane waves and that the seafloor is flat, and then calculated the net electric current element, $\hat{\mathbf{i}}(\omega) = \sigma(\hat{\mathbf{E}}(\omega) + \hat{\mathbf{v}}(\omega) \times \mathbf{F})$, at all the grid points, where the hat denotes a frequency-domain component and $\hat{\mathbf{E}}$ is calculated by Tyler's method. Then, the magnetic field at each grid point was calculated by superposition of magnetic fields from $\hat{\mathbf{i}}(\omega)$ at all the grid points through the Biot–Savart law. This method is very simple and can be used to calculate the magnetic field on land as well as in the ocean. Their simulations demonstrated that the magnetic variation in the Z
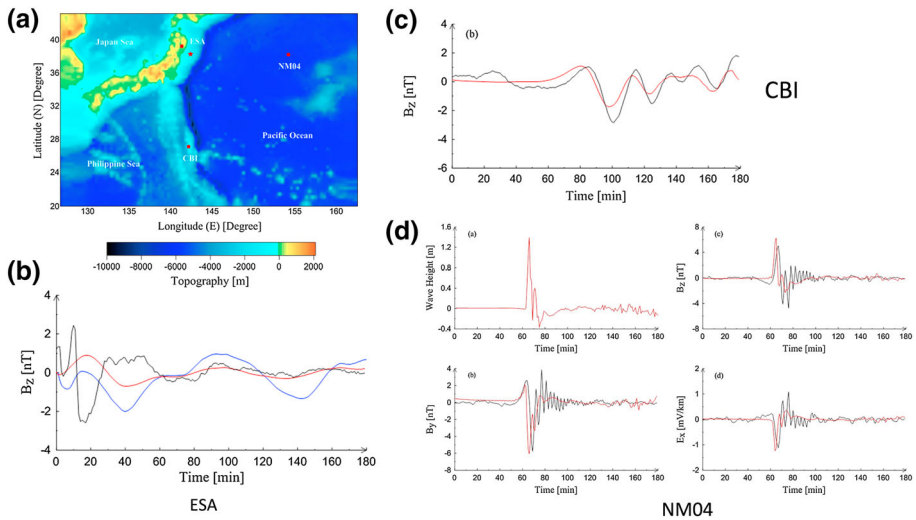
Fig. 5 Results of 3-D numerical simulation of the 2011 Tohoku earthquake tsunami by Zhang et al. (2014b). **a** Locations of the epicenter, land-based magnetic observatories CBI and ESA, and seafloor site NM04. **b** Comparison of the downward component, B_z, at ESA from observations (*black*), as predicted using the Biot–Savart law by Utada et al. (2011) (*red*), and from the 3-D simulation by Zhang et al. (2014b) (*blue*). **c** Comparison of B_z at CBI from observations (*black*) and 3-D simulation (*red*). **d** Comparison of B_y, B_z, and E_x between observations (*black*) and the tsunami simulation result (*red*)

component, same as B_z in this paper, at CBI that preceded the tsunami arrival by ~ 10 min was generated by the 2011 Tohoku earthquake tsunami. Although their results were consistent with observations at CBI for the case of the 2011 Tohoku tsunami, possible errors due to the bathymetry gradient and the curvature of the tsunami waveform should be estimated in the future.

Recently, Kawashima and Toh (2016) used the thin-shell technique (Dawson and Weaver 1979; McKirdy et al. 1985) to successfully reproduce the magnetic field variation observed in the northwest Pacific during the 2007 Kuril earthquake tsunami. This study is discussed in more detail in Sect. 3.4.2 because of its success in constraining the mechanisms of the tsunami and earthquake.

The last decade has seen a variety of new tsunami EM simulation methods. However, most of them are frequency-domain methods. Because most tsunami simulations are performed in the time domain, advances in time-domain simulations will be needed to promote collaborations between tsunami motional induction studies and conventional tsunami simulation studies in the future.

3.4 Applications of Tsunami Electromagnetic Signals

The possible applications of tsunami EM variations to other fields discussed in this section include exploring the internal Earth, inferring the dynamic properties of tsunamis, and developing new seafloor instruments.

3.4.1 Deep Earth Sounding by Tsunami Motional Induction

Although the possibility of exploring the Earth's internal conductivity structure by using EM variations caused by tsunamis has tempted many researchers, Shimizu and Utada (2015) showed that the prospects are dim. They thoroughly investigated the possible use of EM fields generated by surface gravity waves to sound the conductivity structure beneath the seafloor. As the PM mode is dominant in tsunami magnetic phenomena (Sect. 3.2), the Earth's structure can influence tsunami EM signals only through mutual induction between the ocean layer and underlying conductive layers. From their analysis, Shimizu and Utada (2015) concluded that tsunami-generated EM variation observed at the seafloor is suitable only for exploring the tsunami wave properties, not deep Earth structure.

One can see the evidence in Figs. 6 and 7. Shimizu and Utada (2015) compared the amplitudes and phases of tsunami-generated electric and magnetic fields between the case of a realistic 1-D conductivity structure (Fig. 6) and the case of a half-space insulator beneath the seafloor. In Fig. 7, solid and dashed lines denote the cases of $F_z = 30,000$ nT (no F_H) and $F_H = 30,000$ nT (no F_z), respectively. Significant differences in amplitude appear only at periods longer than ~ 5000 s (~ 83 min), which far exceeds the usual tsunami periods of 10–50 min. As for the comparison in phase, at periods less than 5000 s, only small discrepancies appear between the two Earth models, and only in magnetic components. The results in Fig. 7 clearly rule out the use of tsunami-generated EM variations to explore conductivity structures beneath the seafloor.

3.4.2 Constraining Tsunami Dynamic Properties

Although tsunami EM signals are not suitable for exploring Earth's interior, they can be used for investigating tsunami properties. This section describes two notable examples in which tsunami-generated EM fields were used to constrain dynamic parameters of a tsunami and its causative earthquake.
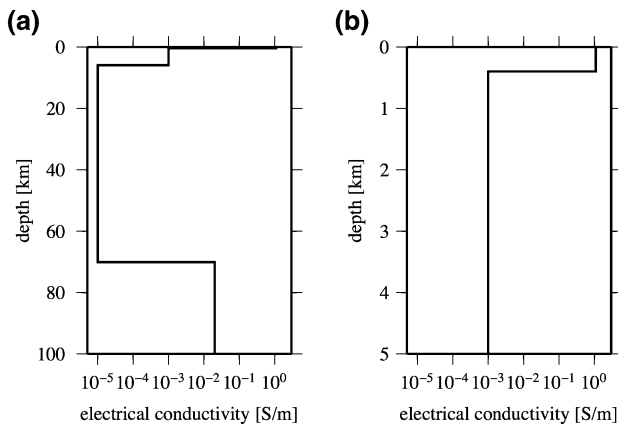
Fig. 6 Electric conductivity profile used in Shimizu and Utada (2015). The sediment layer (1.1 S/m) extends from 0 to 400 m depth below the seafloor, the oceanic crust (10^{-3} S/m) extends to 6 km, the lithospheric mantle (10^{-5} S/m) extends to 70 km, and the conductive mantle or asthenosphere (0.02 S/m) underlies the lithosphere. The ocean depth is 4000 m and consists of seawater (3.3 S/m)
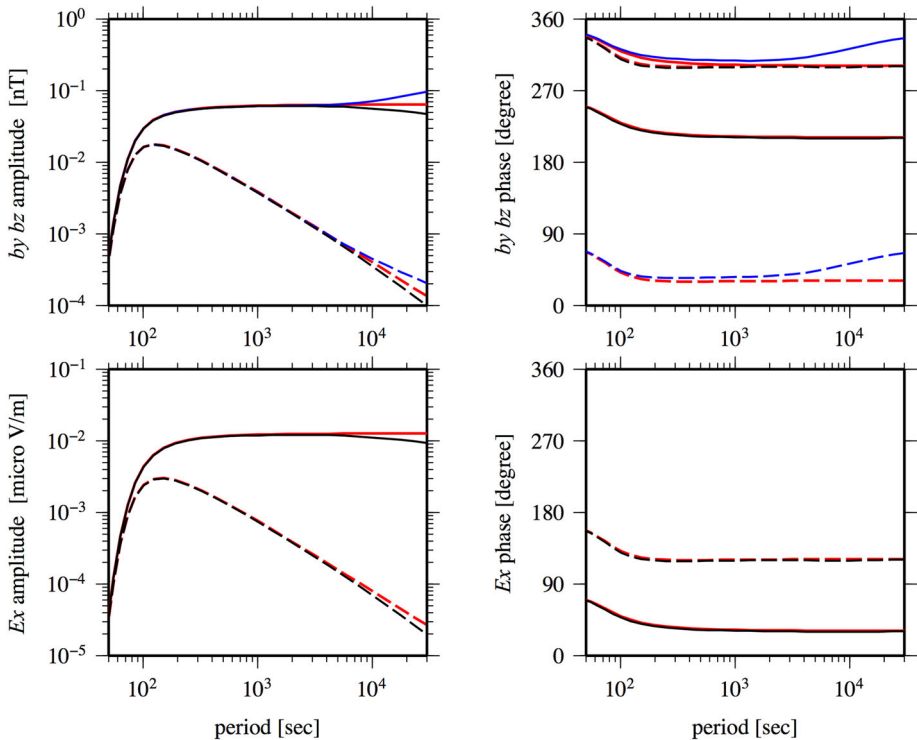
Fig. 7 Relative amplitude and phase of the induced magnetic field (b_y and b_z, top panels) and electric field (Ex, bottom panels) due to a surface gravity wave of 1 cm amplitude for the conductivity models shown in Fig. 6 (Shimizu and Utada 2015). The b_y and b_z components are shown by *blue* and *black lines*, respectively. The ambient field was $F_H = 30,000$ nT ($F_z = 0$ nT) (*dashed lines*) or $F_z = 30,000$ nT ($F_H = 0$ nT) (*solid lines*). For comparison, cases with an insulating sub-seafloor are shown by *red lines*

Ichihara et al. (2013) used the three components of the seafloor magnetic variation data to constrain the tsunami source region for the 2011 Tohoku earthquake. This application was readily feasible because seafloor vector magnetic sensors can monitor the tsunami propagation direction from a single site (Toh et al. 2011). By adopting the back-propagation technique, Ichihara et al. (2013) found that the tsunami reaching the seafloor EM site B14 originated in the region at latitude $\sim$39°N, to the north of regions identified from sea surface displacement data (Maeda et al. 2011). Figure 8 summarizes the back-propagation results (left panels) and the final fit between the observations and simulated results (right panels). A subsequent tsunami source inversion by Satake et al. (2013) confirmed the source region constrained by Ichihara et al. (2013).

Kawashima and Toh (2016) used the linear relationship between the tsunami flow and the tsunami magnetic signals, as shown in Eq. (2), to infer the fault slip model of the 2007 Kuril earthquake that best explains the magnetic variations observed at the north Pacific seafloor. Figure 9 shows the results. As described by Tyler (2015), the ocean is unlike the fluid core or upper atmosphere in that the energy density of the EM field is quite small in comparison with that contained in kinetic and other forms. Given this energy disparity, we may regard oceanic flows as EM sources that are not influenced by EM induction. This stipulation appears as the linear form both in terms of **v** and in terms of **b** in the induction
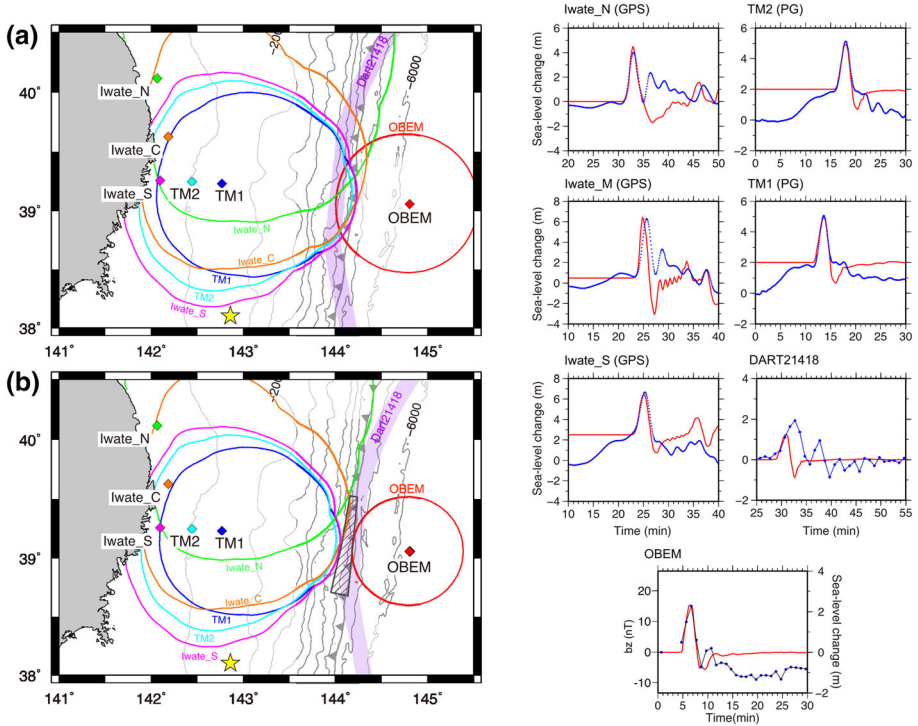
Fig. 8 *Left* Tsunami source area from the 2011 Tohoku earthquake inferred by back-propagation based on vector magnetic field data at the seafloor. *Right* Final fit between observed sea surface displacement and seafloor magnetic data (*blue lines*) and simulated values (*red lines*) (after Ichihara et al. 2013)

equation of Eq. (2), which in turn allows us to calculate Green's functions of the magnetic field at observation sites resulting from a unit slip on each fault segment (Fig. 9b). The linear combination of Green's functions that best explains the observed magnetic data yields a preferred fault model. This method allows magnetic data to easily be incorporated into conventional tsunami source inversions (e.g., Maeda et al. 2011; Satake et al. 2013), a promising advance for future methods to accurately determine tsunami source mechanisms.

3.4.3 Using Seafloor Tsunami EM Signals for Tsunami Early Warning

Recently, the Japan Agency for Marine-Earth Science and Technology (JAMSTEC) developed a seafloor instrument called the Vector TsunaMeter (VTM) that applies seafloor tsunami EM signals to tsunami early warning systems (e.g., JAMSTEC 2014; Marine Technology 2014). A VTM consists of a fluxgate magnetometer for three magnetic field components, a differential pressure gauge (DPG) for the seafloor pressure, and an acoustic modem to transfer data to the sea surface (Fig. 10). Thus the instrument can simultaneously monitor tsunami propagation direction by vector magnetic observations and detect sea surface displacement with the DPG. The VTM communicates with an autonomous wave glider at the sea surface (Liquid Robotics; https://www.liquid-robotics.com/platform/overview/) that can transfer real-time data to land stations via satellite.
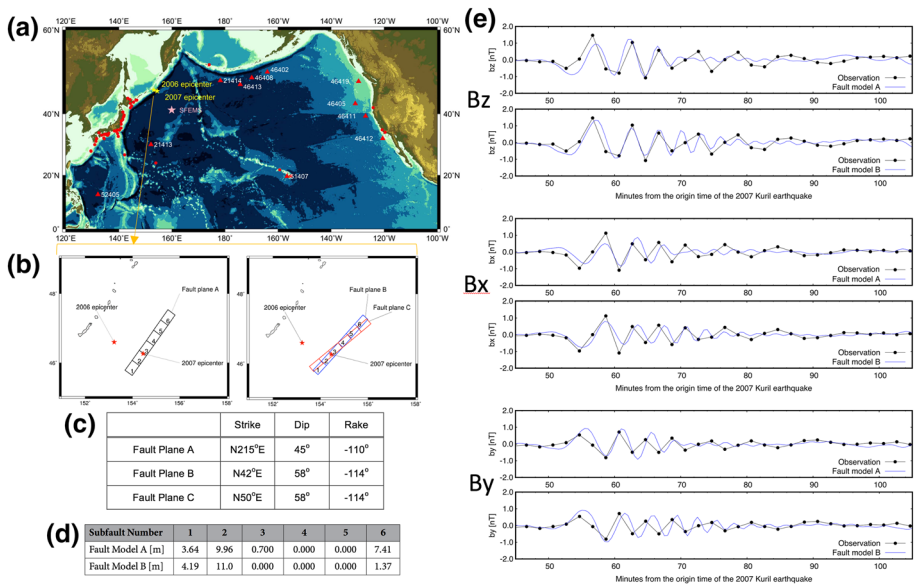
Fig. 9 Fault model for the 2007 Kuril earthquake tsunami inferred from tsunami EM simulations adopting the thin-sheet approximation (Kawashima and Toh 2016). **a** Map of observatories used for tsunami source inversion by Fujii and Satake (2008). **b** Northwest dipping fault model (model A, *left*) and southeast dipping fault plane models (models B and C, *right*). **c** The fault plane parameters of models A, B, and C. **d** Fault slip distributions of models A and B, optimized to fit the seafloor magnetic field in the northwest Pacific. **e** Seafloor magnetic data and calculated values from optimized fault slip distributions of models A and B. From top to bottom, downward, northward, and eastward components are shown
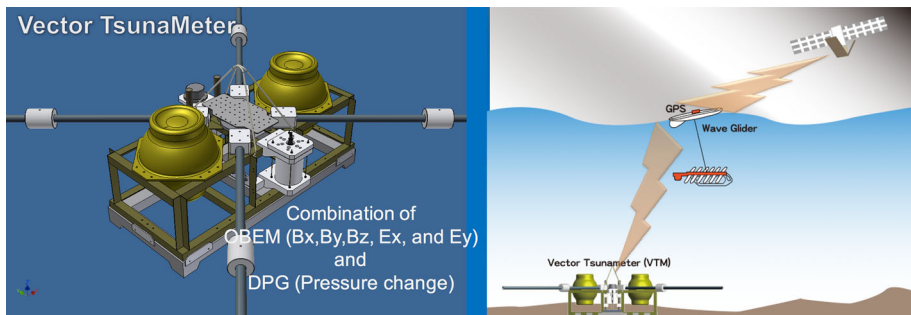
Fig. 10 Schematic drawings of the Vector TsunaMeter (after JAMSTEC 2014)

Hamano et al. (2014a, b) reported successful detection of tsunami EM signals by a VTM installed in the Philippine Sea at the time of the Solomon Islands tsunami (Mw 8.0) of 6 February 2013. Although the combination of a VTM and a wave glider is relatively costly, this technique offers a great advantage in determining the tsunami propagation direction and holds promise as a strategy to prepare for future destructive tsunamis.

4 Motional Induction by Ocean Tides

Studies on motional induction associated with ocean tides have also shown dramatic growth during the last decade. A remarkable feature of tidal motional induction is that it can be observed at the altitude of low-orbit satellites thanks to its spatial scale of ~ 1000 km. In the early 2000s, Tyler et al. (2003) pioneered satellite motional induction studies with satellite observations of M_2 tidal magnetic fields. Sabaka et al. (2015) recently published a global model of the M_2 tidal magnetic field within their magnetic model, Comprehensive Model 5 (CM5), based on more than 12 years of satellite and land-based magnetic data. More recent studies have involved remote monitoring of ocean properties by satellite magnetic observations (e.g., Sabaka et al. 2016; Saynisch et al. 2016).

In contrast to tsunami motional induction, tidal motional induction is attracting interest as a tool to constrain the Earth's internal conductivity structure. For example, Schnepf et al. (2015) investigated the sensitivity of seafloor tidal magnetic fields to upper mantle conductivity, and Grayver et al. (2016) used the M_2 tidal magnetic component at satellite altitudes to infer a new global conductivity model.

This section covers the background of recent advances in tidal motional induction studies in Sect. 4.1 and then describes recent applications in global models of the M_2 tidal magnetic field in Sect. 4.2, remote ocean monitoring in Sect. 4.3, and exploration of the Earth's interior in Sect. 4.4.

4.1 Background

Before 2000, Larsen (1968) and Chave (1983) made notable theoretical and numerical contributions to tidal motional induction studies. Larsen's (1968) initial numerical simulation of tidal EM fields adopted the thin-sheet approximation (e.g., Price 1949) and a Kelvin wave model, in which waves propagate along a straight coastline with exponential decay in the open ocean. Including the self-induction effect appropriately, Larsen (1968) demonstrated M_2 periodicity in magnetic data from some land-based stations due to tidal motional induction. Chave (1983) first pointed out the importance of the TM mode related to the galvanic connection between the ocean layer and the underlying medium by a theoretical analysis using finite conductivities for the crust and upper mantle, which implied that tide-generated horizontal magnetic fields at the seafloor are highly sensitive to the conductivity of underlying layers, whereas TM fields cannot leak upward into the air.

In the 2000s, global simulation approaches became a mainstay of motional induction studies associated with ocean tides, after Tyler et al. (2003) showed that M_2 tidal magnetic fields are detectable by satellites. Their paper calculated the magnetic field of M_2 tidal origin using the tidal model of Egbert and Erofeeva (2002) and adopting the thin-shell approximation with an insulating Earth interior, and successfully compared their prediction with magnetic data observed by the CHAMP satellite.

The effect of sub-seafloor conductivity on tidal magnetic signals started to be investigated with the global integral equation (IE) method after Tyler et al. (2003). The global IE method is capable of including a radial 1-D conductivity structure beneath a laterally heterogeneous surface shell (Kuvshinov et al. 2002; Kuvshinov 2008). With this method, Maus and Kuvshinov (2004), Kuvshinov and Olsen (2005), and Kuvshinov et al. (2006) simulated tide-generated EM fields at the ground level and at low-orbit satellite altitudes with a realistic conductivity structure beneath the seafloor, and they comprehensively

investigated EM fields generated by the N_2, K_1, P_1, and O_1 tidal components as well as the M_2 semidiurnal component. Kuvshinov (2008) reviewed these studies in detail.

The numerical methods introduced by Tyler et al. (2003) and Kuvshinov (2008) became the foundation of later advances. Sabaka et al. (2015) constructed a global model of the M_2 magnetic component and compared it with the forward models of Tyler et al. (2003) and Kuvshinov (2008). The IE method of Kuvshinov (2008) has been chiefly used in studies of the relationships between tidal EM signals and sub-seafloor conductivity (e.g., Schnepf et al. 2014, 2015; Grayver et al. 2016).

4.2 Global Model for the M_2 Tidal Magnetic Field

Magnetic signals related to the tides are relatively easy to observe and extract, especially in long-term datasets, because the tides are stable, global, and precisely known. Since seafloor EM data started to be used in magnetotelluric (MT) studies in the 1960s, the removal (extraction) of tidal signals from the observed data has been of concern not only to researchers involved in motional induction studies but also to those involved in MT surveys, because motional induction by ocean tides generates noise in MT analyses (e.g., Cox 1980). Conventional methods use nighttime data to characterize and extract tidal magnetic components (e.g., Chapman and Miller 1940; Malin and Chapman 1970), whereas some MT studies extract the tidal components directly by the use of sinusoids (e.g., Lizarralde et al. 1995; Baba et al. 2010). A Bayesian tidal analysis program, BAYTAP-G (Ozima et al. 1989), has also been used to extract tidal components (e.g., Segawa and Toh 1992). However, global or regional models of tidal magnetic fields were never constructed from observed magnetic data before Sabaka et al. (2015).

Sabaka et al. (2015) recently added M_2 source parameters in the fifth version, CM5, of their comprehensive geomagnetic field model. As far as I know, CM5 was the first model to provide a global model of the M_2 tidal magnetic field based on observed data. CM5 was derived from more than 12 years of CHAMP, Ørsted, and SAC-C satellite data and hourly mean data from land-based observatories from August 2000 to January 2013 by applying the comprehensive inversion (CI) technique. This technique can decompose observed magnetic fields into variations originating from three different regions: sources beneath the Earth's surface (e.g., electric currents in the core or induced currents in the Earth), sources between the ground and satellite altitudes (e.g., ionospheric sources), and sources above satellite altitudes (e.g., sources in the magnetosphere). Thus, the CI technique coestimates parameters, which are composed of spherical harmonic coefficients for the given time harmonics, for magnetic sources in the magnetosphere, ionosphere, ocean, solid earth, and core (Table 2).

Figure 11 shows good agreement among the results of an inversion for the magnetic field of M_2 origin in CM5 and the forward modeling results of Kuvshinov (2008) and Tyler et al. (2003). Both CM5 and Kuvshinov (2008) used the 1-D conductivity model of Kuvshinov and Olsen (2006), shown on the left side of Fig. 11, and Tyler et al. (2003) assumed an insulating Earth beneath a surface layer with heterogeneous conductance. Figure 12 shows that the R_n spectra (Lowes 1966) of the time-averaged M_2 components for the three models agree quite well up to approximately $n = 18$. The fact that the M_2 field powers in the CM5 and Kuvshinov models are less than those in Tyler's model makes sense because Tyler's model ignores the effect of upper mantle conductivity. The extracted M_2 magnetic component in CM5 should be considered an important reference for a wide range of studies concerned with M_2 ocean tides.

Table 2 Parameterization of geomagnetic model CM5 (after Sabaka et al. 2015)

Field source/effect	# parms	Description	
Core/lithospheric fields	26,960	Spatial: geographic spherical harmonic (SH) $N_{max} = 120$	
		Temporal: order 4 B-splines, 6 month knot spacing from 2000.5 to 2013.0, epoch 2005.0, up to $N_{max} = 20$	
M_2 tidal field	2736	Spatial: geographic SH $N_{max} = 36$	
		Temporal: period of 12.42060122 h, phase fixed with respect to 00:00:00, 1999 January 1 GMT	
Ionospheric/induced fields	5520	Spatial: quasi-dipole (QD) frame, underlying dipole $N_{max} = 60$, $M_{max} = 12$	
		Temporal: annual, semiannual, 24-, 12-, 8- and 6-h periodicities with $F_{10.7}$ scaling plus induction via a priori 3-D conductivity model ('I-D + oceans') and infinite conductor at depth	
Toroidal field	12,240	Spatial: meridional currents in QD frame, underlying dipole SH $N_{max} = 60$, $M_{max} = 12$, one for Ørsted centred at 750 km altitude and one for CHAMP centred at 400 km altitude	
		Temporal: annual, semiannual, 24-, 12-, 8- and 6-h periodicities	
Magnetospheric/induced fields	653,184	Magnetospheric	Spatial: dipole $N_{max} = 1$
			Temporal: discretized in 1-h bins
		Induced	Spatial: dipole $N_{max} = 1$
			Temporal: discretized in 1-h bins
OHM biases	558	One vector bias for each station in local spherical system	
VFM-CRF alignment	1110	Three XYZ-type Euler angles every 10 d for CHAMP, one set of three YZY-type Euler angles for Ørsted	
Total	702,308	–	

Spherical harmonic (SH) coefficients up to degree 36 are included to represent the M_2 tidal signal with the prescribed M_2 period

4.3 Remote Ocean Monitoring by Satellite Observations

Sabaka et al. (2016) presented some exciting possibilities for remote ocean monitoring by using satellite observations of the magnetic field of M_2 tidal origin. They demonstrated that the Swarm satellite constellation enables us to extract tidal magnetic signals at satellite altitude from much shorter observation periods than with the earlier CHAMP satellite (CM5, Sabaka et al. 2015).

The three-satellite Swarm mission, launched by the European Space Agency on November 22, 2013, consists of a pair of satellites flying side by side at a relatively low altitude of approximately 455 km and a single satellite at approximately 515 km (Olsen et al. 2015). The mission enables the use of both along-track and cross-track magnetic field differences in analyses of geomagnetic fields. Exploiting the cross-track magnetic difference between the low-altitude satellite pair, Sabaka et al. (2016) tried to extract magnetic fields generated by semidiurnal tidal components M_2 (period = 12.42060122 h) and N_2 (period = 12.65834751 h) from the first 20.5 months of Swarm data by using the CI technique (Sabaka et al. 2015). They confirmed that extracted magnetic fields of M_2 origin agree well with Tyler's theoretical prediction based on a tidal model of Egbert and Erofeeva (2002), although the weaker N_2 signals were not recovered well. Figure 13
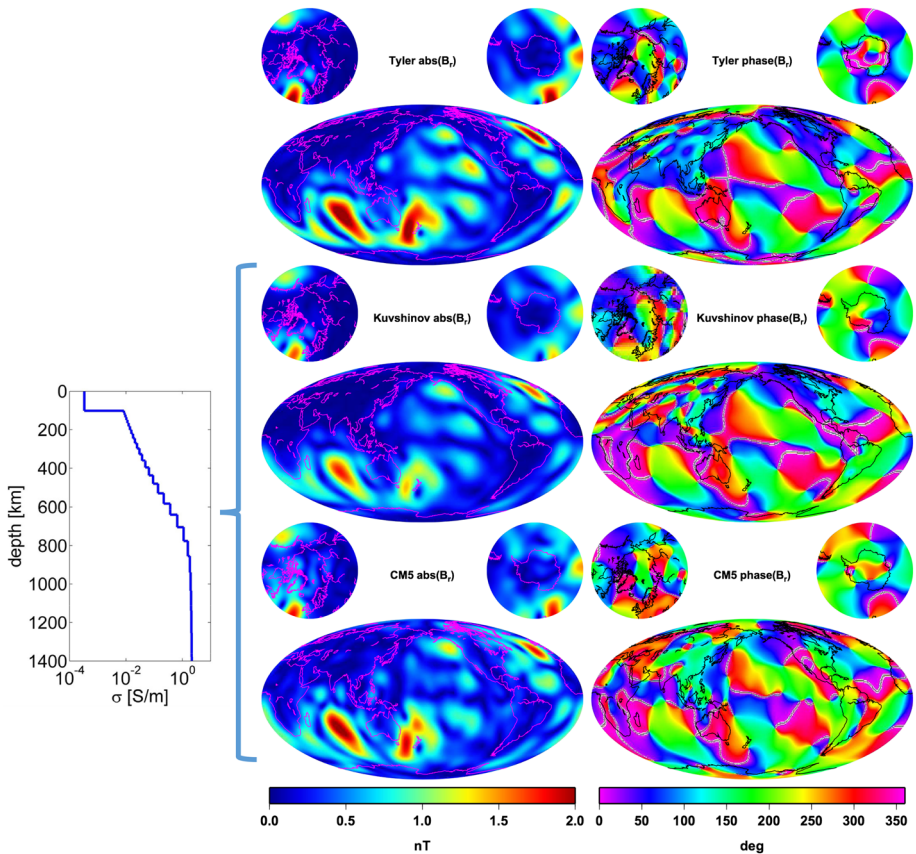
Fig. 11 Outward component of the magnetic field at 430 km altitude generated by the M$_2$ tidal component. Panels from *top to bottom* show the prediction by Tyler et al. (2003), the simulation by Kuvshinov (2008), and the fields obtained by CM5 (Sabaka et al. 2015). *Left* and *right columns* indicate the amplitude and phase of B_r, respectively. Tyler's calculation assumed an insulator beneath the ocean layer, whereas modeling by Kuvshinov and CM5 adopted the 1-D conductivity structure of Kuvshinov and Olsen (2006), shown on the left side (after Sabaka et al. 2015)

summarizes the results of extracting the M$_2$ magnetic field from Swarm and CHAMP satellite data. By using both along-track and cross-track gradient data from the Swarm constellation, Sabaka et al. (2016) extracted an M$_2$ field from 20.5 months of Swarm data that looks much the same as the field extracted from more than 10 years of CHAMP data. This result implies that satellite magnetic observations may enable us to remotely monitor annual and perhaps even seasonal ocean variability.

These promising results have attracted the attention of oceanographers and climatologists because they offer the possibility of using satellite magnetic observations to monitor ocean parameters dependent on climate changes. Recently, Saynisch et al. (2016) used 3-D forward modeling to investigate the effect of decay in the Antarctic meridional overturning circulation (AMOC) on the magnetic field generated by the M$_2$ tidal component. AMOC decay is an expected result of the increase in freshwater input with melting of Greenland glaciers (e.g., Stouffer et al. 2006). Saynisch et al. (2016) demonstrated that the tide-generated magnetic fields are likely to be influenced not by changes in the tide system (i.e.,
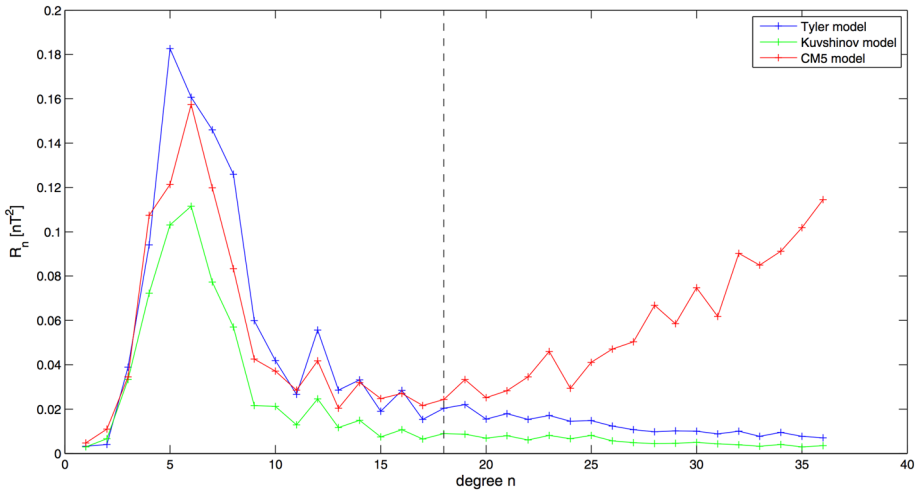
Fig. 12 R_n spectra (Lowes 1966) of the time-averaged oceanic M_2 tidal magnetic field at Earth's surface ($r = 6371.2$ km) from $n = 1$–36 for the three models shown in Fig. 11 (after Sabaka et al. 2015)

seawater velocities), but by changes in seawater salinity and temperature. The expected variability of the outward magnetic field at the sea surface was ∼0.7 nT. Investigations of this kind, then, can give us important information for predicting future M_2 magnetic signals.

4.4 Deep Earth Sounding by Tide-Generated EM Fields

In the late 1960s, Larsen noted, "Electromagnetic variations induced by oceanic tides depend on the distribution of tidal currents and on the distribution of electrical conductivity beneath the ocean. If either were known perfectly, the measurements would serve to give some precise information of the other" (Larsen 1968, p. 47). Unlike the case with tsunami magnetic signals (Sect. 3.4.1), the possibilities are great for exploring Earth's interior by using the EM fields generated by ocean tides. It is also noteworthy that Chave (1983) pointed out the importance of the TM mode in tidally induced seafloor EM fields, a point of growing relevance in recent studies of tidally induced EM variations. Kuvshinov et al. (2006) were the first to try to constrain the Earth's conductivity structure exploiting tidal motional induction. They suggested the resistance of 100-km lithosphere in the range of 10^8 and 10^9 Ωm^2 from comparisons between electrical voltage data over submarine cables and simulated results for the M_2 tidal component.

Dostal et al. (2012) performed numerical modeling for only the TM component of the magnetic field associated with the M_2 tide and found that the energy of the TM magnetic component is concentrated in short-wavelength spatial patterns over the shallow waters of coastal regions.

Adopting the approach of Kuvshinov (2008), Schnepf et al. (2014) compared seafloor observations with the calculated magnetic fields originating from the M_2, N_2, and O_1 components of ocean tides by specifying models with variable conductivity structure (Baba et al. 2010; Kuvshinov and Olsen 2006; Shimizu et al. 2010). In their result for the M_2 tidal component (Fig. 14), the differences in the adopted 1-D conductivity models are seen to substantially influence the estimated magnetic components at seafloor observatories.
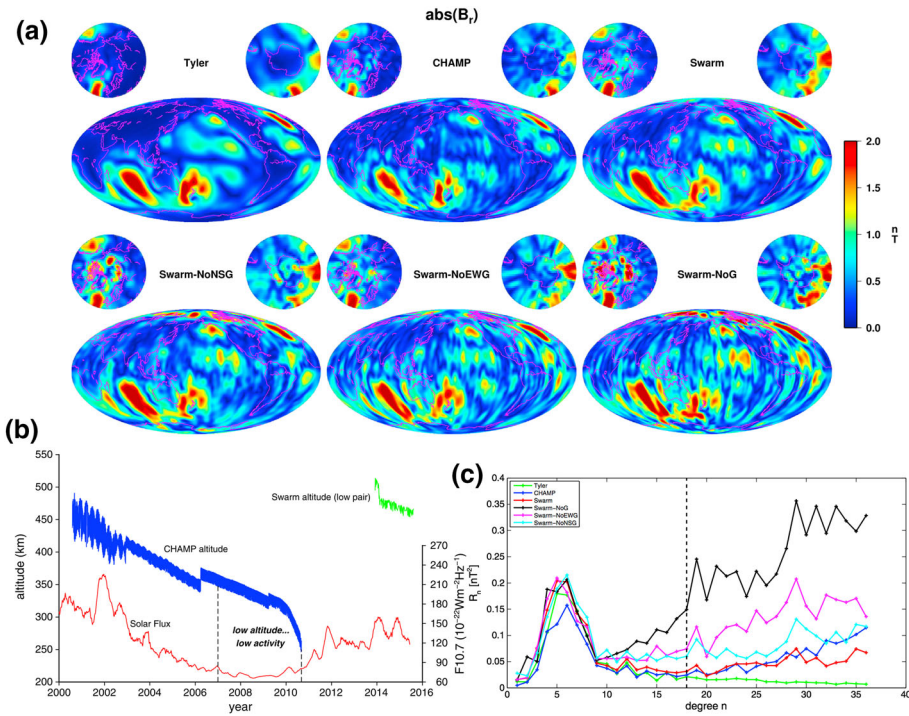
Fig. 13 **a** B_r amplitudes generated by the M_2 tidal component at 430 km altitude from the forward calculation by Tyler et al. (2003) (*top left*), the comprehensive inversion (CI) from CHAMP data (*top center*), the CI from Swarm data with full gradients data (*top right*), the CI from Swarm data without along-track gradients (*bottom left*), the CI from Swarm data without cross-track gradient (*bottom center*), and the CI from Swarm data without any gradients (*bottom right*). **b** Altitude time lines for the CHAMP and Swarm satellites along with the solar activity (F10.7) index. **c** R_n spectra of each spherical harmonic degree n among the six results presented in **a**. After Sabaka et al. (2016)

Schnepf et al. (2015) used numerical experiments to investigate whether motional induction due to ocean tides is useful for exploring Earth's interior. The results of their sensitivity study are summarized in Fig. 15. They compared Frobenius norms of tide-generated EM components,

$$\left| S_F^{l,k} \right| = \left(\sum_{i,j} \left| F_{i,j}^{l,k} - F_{i,j}^{l,1} \right|^2 \right), \tag{8}$$

among several 1-D conductivity structure scenarios. In Eq. (8), F is the corresponding field component, i, j specify grid points in or above oceanic regions, k represents the conductivity scenario (C1, C2, C3, C4, C5) listed in Fig. 15b, and l is the layer being analyzed. This investigation showed that the horizontal magnetic field at the seafloor, B_h, is remarkably sensitive to the lithospheric conductivity. This sensitivity was attributed to the galvanic coupling between the source region (the ocean layer) and the sub-seafloor medium. Although Schnepf et al. (2015) did not show the spatial distribution of the sensitivity of B_h, the work of Dostal et al. (2012) suggests that the sensitivity would be relatively high
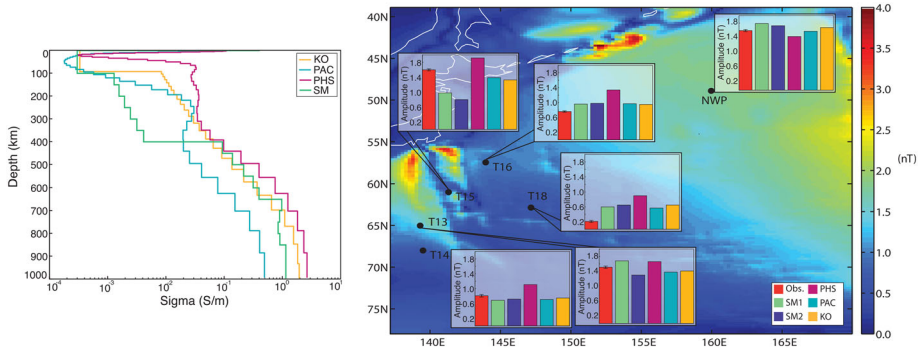
Fig. 14 Comparison of magnetic amplitudes generated by the M_2 tidal component, $\mathbf{B} \cdot \mathbf{B}^m / |\mathbf{B}^m|$, where $\mathbf{B}$ is the tide-generated magnetic field and $\mathbf{B}^m$ is the ambient main field. Color bars correspond to observations (red bar) and numerical predictions using the four 1-D conductivity structures shown in the left panel. KO is the model of Kuvshinov and Olsen (2006), PAC and PHS are the Pacific and Philippine Sea models of Baba et al. (2010), respectively, and SM is the model of Shimizu et al. (2010). All numerical predictions were calculated on a global grid of $0.25° \times 0.25°$ resolution, except the SM2 model, for which the SM model was used on a grid of $1° \times 1°$ resolution (after Schnepf et al. 2014)
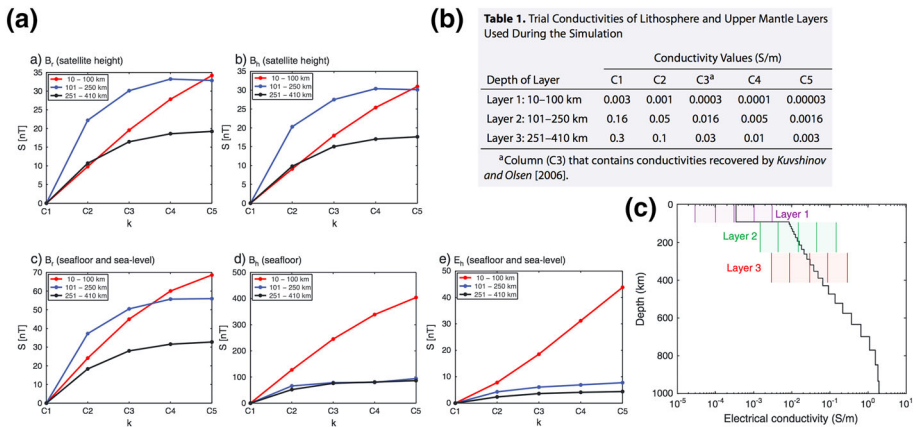
Fig. 15 Sensitivity of tide-generated EM variations to the underlying conductivity structure. **a** Panels **a** to **e** show the sensitivity of the outward and horizontal components (B_r and B_h) at a satellite altitude of 430 km, B_r and B_h at the seafloor, and the horizontal component of the electric field at sea level (E_h), respectively. The sensitivity, S, is defined by the Frobenius norm from Eq. 8. **b** List of conductivity values for the three layers in models C1 to C5. **c** Graph showing values of conductivity in the three layers of models C1 to C5 (after Schnepf et al. 2015)

in coastal regions. This implies that ocean tidal flows might be efficient sources of data to infer deep conductivity structures, especially in some coastal regions.

Grayver et al. (2016) recently demonstrated the feasibility of using the M_2 tidal field to explore Earth's interior by inferring a new global conductivity model from the radial component of M_2 tidal magnetic data at satellite altitude. They used the IE method (Kuvshinov 2008) and the Hamburg direct data Assimilation Methods for TIDes (HAMTIDE) ocean tidal model (Taguchi et al. 2014) to calculate the M_2 tidal magnetic field at an

altitude of 430 km and applied a stochastic optimization technique (Grayver and Kuvshinov 2016) to invert a new global 1-D electrical conductivity model. The M_2 magnetic data were prepared from CM5 (Sabaka et al. 2015) using more than 12 years of satellite magnetic data. Here, one may get concerned about effects of the 1-D structure used in CM5 (see Fig. 11) on the new one inverted by Grayver et al. (2016). Certainly, CM5 coestimated the parameters with a 1-D conductivity model prescribed for induction due to ionospheric sources. However, the induced magnetic fields due to ionospheric disturbances with periodicity close to the M_2 component did not affect the extracted M_2 component, because the extraction of M_2 signals by CM5 was nearly the same as a data selection with a rigid M_2 period (T. J. Sabaka and R. H. Tyler, pers. comm., August 2016). The inversion by Grayver et al. (2016) succeeded in placing the lithosphere–asthenosphere boundary at a depth of ~ 72 km (Fig. 16). Their method supplied a new approach to constrain the conductivity of the upper mantle. Although Grayver et al. (2016) used only tidal magnetic signals at satellite altitude, seafloor tidal EM fields must be much more sensitive to the sub-seafloor conductivity, as pointed by Schnepf et al. (2015). Inversions using tidal EM data from the seafloor may be expected in the near future.
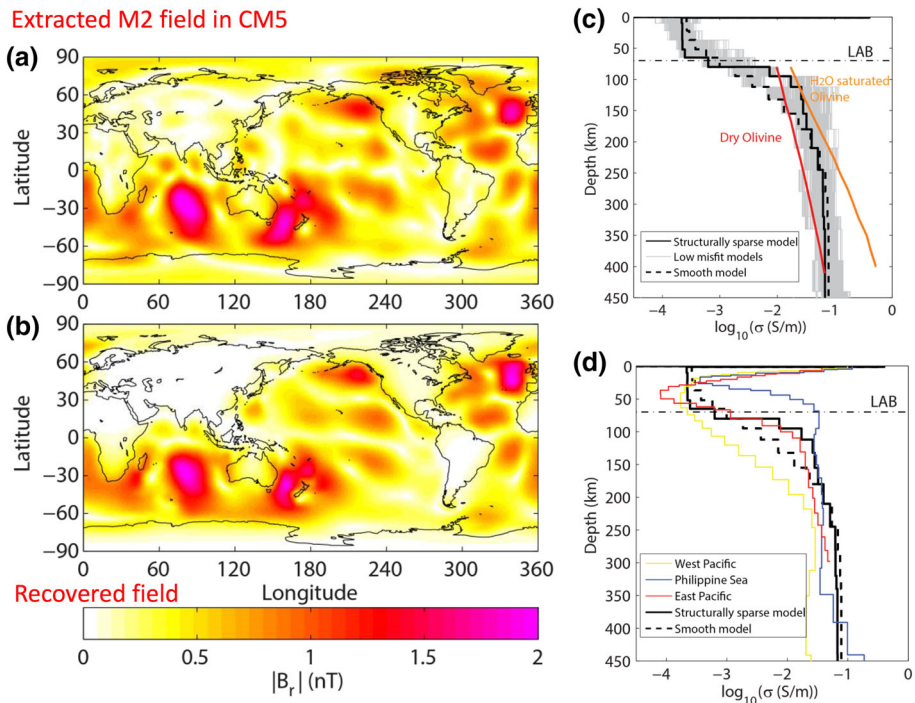
Fig. 16 Results of global 1-D conductivity inversion using the M_2 tidal magnetic field at 430 km altitude (Grayver et al. 2016). **a** Amplitude of the radial component of the M_2 tidal magnetic field extracted by CM5 (Sabaka et al. 2015). **b** The recovered field from the inversion. **c** Inverted 1-D models: smooth model (*dashed line*) and sparse model that permits conductivity jumps (*solid line*). The *gray lines* represent 1000 models for which the misfit from the final models is no more than 10%. LAB, lithosphere–asthenosphere boundary. Conductivities of dry and water-saturated olivine (Katsura and Yoshino 2015) are shown by *red* and *orange lines*, respectively. **d** Comparison with other 1-D conductivity structures. The models from the Philippine Sea Plate (*blue line*) and the West Pacific region (*yellow line*) are from Baba et al. (2010), and the model from the East Pacific region (*red line*) is after Sarafian et al. (2015)

5 Summary

5.1 Progress in Tsunami Motional Induction Studies

1. Large numbers of EM data associated with tsunami motional induction have been reported during the last decade (e.g., Toh et al. 2011; Manoj et al. 2011; Utada et al. 2011; Suetsugu et al. 2012; Minami and Toh 2013; Sugioka et al. 2014; Zhang et al. 2014a, b; Schnepf et al. 2016).
2. The theory of tsunami motional induction has been recently revisited by many researchers (e.g., Ichihara et al. 2013; Sugioka et al. 2014; Minami et al. 2015; Shimizu and Utada 2015).
3. Tsunami EM signals have been shown to depend strongly on the ocean depth (Minami et al. 2015).
4. Several new types of numerical techniques have appeared for the simulation of tsunami-generated magnetic fields, including a 2-D time-domain method (Minami and Toh 2013), a 3-D frequency-domain IE technique (Zhang et al. 2014b), a combination of Biot–Savart and Tyler's analytical solution (Tatehata et al. 2015), and a thin-shell 3-D frequency technique (Kawashima and Toh 2016).
5. It has been established that signals from tsunami motional induction are not useful for exploration of the Earth's interior (Shimizu and Utada 2015).
6. The development of the Vector TsunaMeter (VTM) in combination with real-time data transmission by an autonomous wave glider is a promising approach for applying tsunami EM signals to tsunami early warning (Hamano et al. 2014a, b; JAMSTEC 2014; Marine Technology 2014).
7. Seafloor tsunami magnetic data have been successfully used to constrain earthquake and tsunami mechanisms (Ichihara et al. 2013; Kawashima and Toh 2016). The linear relationship between seawater velocity and the EM fields they generate enable us to easily apply magnetic data to conventional tsunami source inversions.

5.2 Progress in Studies of Motional Induction Due to Ocean Tides

1. A global model of the M_2 tidal magnetic field has resulted from the addition of M_2 tidal source parameters to geomagnetic field model CM5 (Sabaka et al. 2015). Many global simulation studies associated with ocean tides (Maus and Kuvshinov 2004; Kuvshinov and Olsen 2005; Kuvshinov et al. 2006; Dostal et al. 2012; Saynisch et al. 2016) have followed the pioneering work of Tyler et al. (2003).
2. Motional induction by ocean tides has the potential to be used to explore the Earth's interior (Schnepf et al. 2014, 2015).
3. The seafloor horizontal magnetic component of M_2 tidal origin is highly sensitive to the conductivity beneath the seafloor because of the galvanic (TM mode) coupling between the ocean layer and the sub-seafloor medium (Schnepf et al. 2015).
4. The Swarm constellation mission allows us to extract the M_2 tidal magnetic component from relatively short magnetic data records, which may make it possible to monitor annual and seasonal variations of seawater temperature and salinity through M_2 tidal magnetic signals (Sabaka et al. 2016; Saynisch et al. 2016).
5. Exploration of the Earth's interior using tide-generated magnetic data from satellite altitudes has been demonstrated (Grayver et al. 2016).

References

Adams AJ (1881) Earth currents. Part 2. J Soc Telegraph Eng Electr 10(35):34–44

Andres M, Jan S, Sanford T et al (2015) Mean structure and variability of the Kuroshio from northeastern Taiwan to southwestern Japan. Oceanography 28:84–95. doi:10.5670/oceanog.2015.84

Baba K, Utada H, Goto T et al (2010) Electrical conductivity imaging of the Philippine Sea upper mantle using seafloor magnetotelluric data. Phys Earth Planet Inter 183:44–62. doi:10.1016/j.pepi.2010.09.010

Bernard EN, Meinig C (2011) History and future of deep-ocean tsunami measurements. In: OCEANS'11 MTS/IEEE KONA. IEEE, pp 1–7

Chapman S, Miller J (1940) The statistical determination of lunar daily variations in geomagnetic and meteorological elements. Geophys Suppl Mon Not R Astron Soc 4:649–669

Chave AD (1983) On the theory of electromagnetic induction in the earth by ocean currents. J Geophys Res 88:3531–3542

Chave AD (1984) On the electromagnetic fields induced by oceanic internal waves. J Geophys Res 89:10519. doi:10.1029/JC089iC06p10519

Chave AD, Luther DS (1990) Low-frequency, motionally induced electromagnetic fields in the ocean 1. Theory. J Geophys Res 95:7185–7200

Constable S (2013) Review paper: Instrumentation for marine magnetotelluric and controlled source electromagnetic sounding. Geophys Prospect 61:505–532. doi:10.1111/j.1365-2478.2012.01117.x

Cox C (1980) Electromagnetic induction in the oceans and inferences on the constitution of the earth. Geophys Surv 4:137–156. doi:10.1007/BF01452963

Cox C, Kroll N, Pistek P, Watson K (1978) Electromagnetic fluctuations induced by wind waves on the deep-sea floor. J Geophys Res 83:431. doi:10.1029/JC083iC01p00431

Dawson TW, Weaver JT (1979) Three-dimensional induction in a non-uniform thin sheet at the surface of a uniformly conducting earth. Geophys J Int 59:445–462. doi:10.1111/j.1365-246X.1979.tb02566.x

Dostal J, Martinec Z, Thomas M et al (2012) The modelling of the toroidal magnetic field induced by tidal ocean circulation. Geophys J Int 189:782–798. doi:10.1111/j.1365-246X.2012.05407.x

Egbert GD, Erofeeva SY (2002) Efficient inverse modeling of barotropic ocean tides. J Atmos Ocean Technol 19:183–204. doi:10.1175/1520-0426(2002)019<0183:EIMOBO>2.0.CO;2

Egedal J (1937) On the lunar-diurnal variation in the earth-currents. Terr Magn Atmos Electr 42:179–181. doi:10.1029/TE042i002p00179

Egedal J (1948) The lunar-diurnal variation in the earth-currents at the Italian Polar Year Station at Mogadiscio, Somaliland. Geofis Pura e Appl 11:1–7. doi:10.1007/BF01980420

Faraday M (1832) The bakerian lecture: experimental researches in electricity. Second series. Philos Trans R Soc Lond 122:163–194

Filloux JH (1967) An ocean bottom, D component magnetometer. Geophysics 32:978–987. doi:10.1190/1.1439910

Filloux JH (1973) Techniques and instrumentation for study of natural electromagnetic induction at sea. Phys Earth Planet Inter 7:323–338. doi:10.1016/0031-9201(73)90058-7

Filloux J (1987) Instrumentation and experimental methods for oceanic studies. Geomagnetism 1:143–248

Flosadóttir ÁH, Larsen JC, Smith JT (1997) Motional induction in North Atlantic circulation models. J Geophys Res Oceans 102:10353–10372. doi:10.1029/96JC03603

Fraser DC (1966) The magnetic fields of ocean waves. Geophys J Int 11(5):507–517

Frick P, Baliunas SL, Galyagin D et al (1997) Wavelet analysis of stellar chromospheric activity variations. Astrophys J 483:426–434. doi:10.1086/304206

Fujii I, Chave AD (1999) Motional induction effect on the planetary-scale geoelectric potential in the eastern North Pacific. J Geophys Res Oceans 104:1343–1359. doi:10.1029/1998JC900041

Fujii Y, Satake K (2008) Tsunami sources of the November 2006 and January 2007 great Kuril earthquakes. Bull Seismol Soc Am 98:1559–1571. doi:10.1785/0120070221

Grayver AV, Kuvshinov AV (2016) Exploring equivalence domain in nonlinear inverse problems using Covariance Matrix Adaption Evolution Strategy (CMAES) and random sampling. Geophys J Int 205:971–987. doi:10.1093/gji/ggw063

Grayver AV, Schnepf NR, Kuvshinov AV, Sabaka TJ, Manoj C, Olsen N (2016) Satellite tidal magnetic signals constrain oceanic lithosphere-asthenosphere boundary. Sci Adv 2(9):e1600798

Hamano Y, Sugioka H, Tada N et al (2014a) Detection of micro-tsunamis by using Vector Tsunameter. 2014 SGEPSS Fall Meet R003-4

Hamano Y, Sugioka H, Toh H (2014b) Long-term deployment of Wave Glider for a real-time tsunami monitoring system using the Vector Tsunameter. Japan Geoscience Union Meet 2014 HDS27-08

Harvey RR, Larsen JC, Montaner R (1977) Electric field recording of tidal currents in the Strait of Magellan. J Geophys Res 82:3472–3476. doi:10.1029/JC082i024p03472

Ichihara H, Hamano Y, Baba K, Kasaya T (2013) Tsunami source of the 2011 Tohoku earthquake detected by an ocean-bottom magnetometer. Earth Planet Sci Lett 382:117–124

Irrgang C, Saynisch J, Thomas M (2016a) Impact of variable seawater conductivity on motional induction simulated with an ocean general circulation model. Ocean Sci 12:129–136. doi:10.5194/os-12-129-2016

Irrgang C, Saynisch J, Thomas M (2016b) Ensemble simulations of the magnetic field induced by global ocean circulation: estimating the uncertainty. J Geophys Res Oceans 121:1866–1880. doi:10.1002/2016JC011633

JAMSTEC (2014) Real-time ocean bottom tsunami monitoring system using vector TsunaMeter successfully completes trial observation. In: Press release 4 April 2014. http://www.jamstec.go.jp/e/about/press_release/20140404/. Accessed 8 May 2017

Junge A (1988) The telluric field in northern Germany induced by tidal motion in the North Sea. Geophys J Int 95:523–533. doi:10.1111/j.1365-246X.1988.tb06701.x

Kasaya T, Goto T (2009) A small ocean bottom electromagnetometer and ocean bottom electrometer system with an arm-folding mechanism (technical report). Explor Geophys 40:41. doi:10.1071/EG08118

Katsura T, Yoshino T (2015) Heterogeneity of electrical conductivity in the oceanic upper mantle. In: Khan A, Deschamps F (eds) The Earth's heterogeneous mantle. Springer International Publishing, Cham, pp 173–204

Kawakatsu H, Baba K, Takeo A, Isse T, Shiobara H, Utada H (2013) In-situ characterization of the lithosphere/asthenosphere system of the 'normal oceanic mantle' via ocean bottom geophysical observations: first results of the NOMan project. In AGU fall meeting abstracts

Kawashima I, Toh H (2016) Tsunami-generated magnetic fields may constrain focal mechanisms of earthquakes. Sci Rep 6:28603. doi:10.1038/srep28603

Kherani EA, Rolland L, Lognonné P et al (2016) Traveling ionospheric disturbances propagating ahead of the Tohoku-Oki tsunami: a case study. Geophys J Int 204:1148–1158. doi:10.1093/gji/ggv500

Klausner V, Mendes O, Domingues MO et al (2014) Advantage of wavelet technique to highlight the observed geomagnetic perturbations linked to the Chilean tsunami (2010). J Geophys Res Sp Phys 119:3077–3093. doi:10.1002/2013JA019398

Klausner V, Kherani EA, Muella MTAH (2016) Near- and far-field tsunamigenic effects on the Z component of the geomagnetic field during the Japanese event, 2011. J Geophys Res Sp Phys 121:1772–1779. doi:10.1002/2015JA022173

Kuvshinov AV (2008) 3-D global induction in the oceans and solid Earth: recent progress in modeling magnetic and electric fields from sources of magnetospheric, ionospheric and oceanic origin. Surv Geophys 29:139–186. doi:10.1007/s10712-008-9045-z

Kuvshinov A, Olsen N (2005) 3-D modelling of the magnetic fields due to ocean tidal flow. In: Reigber C, Lühr H, Schwintzer P, Wickert J (eds) Earth observation with CHAMP. Springer, Berlin, pp 359–365

Kuvshinov A, Olsen N (2006) A global model of mantle conductivity derived from 5 years of CHAMP, Ørsted, and SAC-C magnetic data. Geophys Res Lett. doi:10.1029/2006GL027083

Kuvshinov AV, Avdeev DB, Pankratov OV et al (2002) Modelling electromagnetic fields in a 3D spherical earth using a fast integral equation approach. Methods Geochem Geophys 35:43–54. doi:10.1016/S0076-6895(02)80085-3

Kuvshinov A, Junge A, Utada H (2006) 3-D modelling the electric field due to ocean tidal flow and comparison with observations. Geophys Res Lett 33:L06314. doi:10.1029/2005GL025043

Larsen JC (1968) Electric and magnetic fields induced by deep sea tides. Geophys J Int 16:47–70. doi:10.1111/j.1365-246X.1968.tb07135.x

Larsen J (1971) The electromagnetic field of long and intermediate water waves. J Mar Res 29:28–45

Larsen JC (1992) Transport and heat flux of the Florida current at 27 degrees N derived from cross-stream voltages and profiling data: theory and observations. Philos Trans Royal Society London A: Math Phys Eng Sci 338(1650):169–236

Larsen J, Cox C (1966) Lunar and solar daily variation in the magnetotelluric field beneath the ocean. J Geophys Res 71:4441–4445. doi:10.1029/JZ071i018p04441

Larsen J, Sanford T (1985) Florida current volume transports from voltage measurements. Science 227:302–304

Lilley FEM, Filloux JH, Mulhearn PJ, Ferguson IJ (1993) Magnetic signals from an ocean eddy. J Geomagn Geoelectr 45:403–422. doi:10.5636/jgg.45.403

Lilley FEM, Hitchman AP, Milligan PR et al (2004) Sea-surface observations of the magnetic signals of ocean swells. Geophys J Int 159:565–572. doi:10.1111/j.1365-246X.2004.02420.x

Lizarralde D, Chave A, Hirth G, Schultz A (1995) Northeastern Pacific mantle conductivity profile from long-period magnetotelluric sounding using Hawaii-to-California submarine cable data. J Geophys Res Solid Earth 100:17837–17854. doi:10.1029/95JB01244

Longuet-Higgins MS (1949) The electrical and magnetic effects of tidal streams. Geophys J Int 5:285–307. doi:10.1111/j.1365-246X.1949.tb02945.x

Longuet-Higgins MS, Stern ME, Stommel HM (1954) The electrical field induced by ocean currents and waves, with applications to the method of towed electrodes. Massachusetts Institute of Technology and Woods Hole Oceanographic Institution, Cambridge

Lowes FJ (1966) Mean-square values on sphere of spherical harmonic vector fields. J Geophys Res 71:2179. doi:10.1029/JZ071i008p02179

Luther DS, Chave AD, Filloux JH (1987) BEMPEX: a study of barotropic ocean currents and lithospheric electrical conductivity. EOS Trans Am Geophys Union 68:618. doi:10.1029/EO068i027p00618

Luther DS, Filloux JH, Chave AD (1991) Low-frequency, motionally induced electromagnetic fields in the ocean: 2. Electric field and Eulerian current comparison. J Geophys Res 96:12797. doi:10.1029/91JC00884

Maclure KC, Hafer RA, Weaver JT (1964) Magnetic variations produced by ocean swell. Nature 204:1290–1291. doi:10.1038/2041290a0

Maeda T, Furumura T, Sakai S, Shinohara M (2011) Significant tsunami observed at ocean-bottom pressure gauges during the 2011 off the Pacific coast of Tohoku Earthquake. Earth Planets Sp 63:803–808. doi:10.5047/eps.2011.06.005

Malin SRC, Chapman S (1970) The determination of lunar daily geophysical variations by the Chapman–Miller method. Geophys J Int 19:15–35. doi:10.1111/j.1365-246X.1970.tb06738.x

Malkus W, Stern M (1952) Determination of ocean transports and velocities by electromagnetic effects. J Mar Res 11:97–105

Manoj C, Kuvshinov A, Maus S, Lühr H (2006) Ocean circulation generated magnetic signals. Earth Planets Sp 58:429–437. doi:10.1186/BF03351939

Manoj C, Kuvshinov A, Neetu S, Harinarayana T (2010) Can undersea voltage measurements detect tsunamis? Earth Planets Sp 62:353–358. doi:10.5047/eps.2009.10.001

Manoj C, Maus S, Chulliat A (2011) Observation of magnetic fields generated by tsunamis. EOS Trans Am Geophys Union 92:13. doi:10.1029/2011EO020002

Marine Technology (2014) Realtime tsunami monitoring in Japan. http://magazines.marinelink.com/tags/technology/tsunami-detection-technology. Accessed 8 May 2017

Maus S, Kuvshinov A (2004) Ocean tidal signals in observatory and satellite magnetic measurements. Geophys Res Lett 31:L15313. doi:10.1029/2004GL020090

McKirdy DM, Weaver JT, Dawson TW (1985) Induction in a thin sheet of variable conductance at the surface of a stratified earth: II. Three-dimensional theory. Geophys J Int 80:177–194. doi:10.1111/j.1365-246X.1985.tb05084.x

Minami T, Toh H (2013) Two-dimensional simulations of the tsunami dynamo effect using the finite element method. Geophys Res Lett 40:4560–4564

Minami T, Toh H, Tyler RH (2015) Properties of electromagnetic fields generated by tsunami first arrivals: classification based on the ocean depth. Geophys Res Lett 42:2171–2178. doi:10.1002/2015GL063055

Nolasco R, Soares A, Dias JM et al (2006) Motional induction voltage measurements in estuarine environments: the Ria de Aveiro Lagoon (Portugal). Geophys J Int 166:126–134. doi:10.1111/j.1365-246X.2006.02936.x

Ochadlick AR (1989) Measurements of the magnetic fluctuations associated with ocean swell compared with Weaver's Theory. J Geophys Res 94:16237. doi:10.1029/JC094iC11p16237

Olsen N, Hulot G, Lesur V et al (2015) The Swarm initial field model for the 2014 geomagnetic field. Geophys Res Lett 42:1092–1098. doi:10.1002/2014GL062659

Ozima M, Mori T, Takayama H (1989) Observation of earth-potential using telegraphic facilities and analysis with BAYTAP-G. J Geomagn Geoelectr 41:945–962. doi:10.5636/jgg.41.945

Palshin NA (1996) Oceanic electromagnetic studies: a review. Surv Geophys 17:455–491. doi:10.1007/BF01901641

Petersen RA, Poehls KA (1982) Model spectrum of magnetic induction caused by ambient internal waves. J Geophys Res 87:433. doi:10.1029/JC087iC01p00433

Podney W (1975) Electromagnetic fields generated by ocean waves. J Geophys Res 80:2977–2990. doi:10.1029/JC080i021p02977

Podney W, Sager R (1979) Measurement of fluctuating magnetic gradients originating from oceanic internal waves. Science 205(4413):1381–1382

Price A (1949) The induction of electric currents in non-uniform thin sheets and shells. Q J Mech Appl Math 2:283–310

Rooney WJ (1938) Lunar diurnal variation in Earth-currents at Huancayo and Tucson. J Geophys Res 43:107. doi:10.1029/TE043i002p00107

Sabaka TJ, Olsen N, Tyler RH, Kuvshinov A (2015) CM5, a pre-Swarm comprehensive geomagnetic field model derived from over 12 yr of CHAMP, Orsted, SAC-C and observatory data. Geophys J Int 200:1596–1626. doi:10.1093/gji/ggu493

Sabaka TJ, Tyler RH, Olsen N (2016) Extracting ocean-generated tidal magnetic signals from *Swarm* data through satellite gradiometry. Geophys Res Lett 43:3237–3245. doi:10.1002/2016GL068180

Sanford TB (1971) Motionally induced electric and magnetic fields in the sea. J Geophys Res 76:3476–3492. doi:10.1029/JC076i015p03476

Sanford TB, Drever RG, Dunlap JH (1978) A velocity profiler based on the principles of geomagnetic induction. Deep Sea Res 25:183–210. doi:10.1016/0146-6291(78)90006-1

Sanford TB, Drever RG, Dunlap JH, D'Asaro EA (1982) Design, operation and performance of an expendable temperature and velocity profiler (XTVP) (No. APL-UW-8110). Washington univ seattle applied physics lab

Sanford TB, Driver RG, Dunlap JH et al (1985) An acoustic Doppler and electromagnetic velocity profiler. J Atmos Ocean Technol 2:110–124. doi:10.1175/1520-0426(1985)002<0110:AADAEV>2.0.CO;2

Sanford TB, Dunlap JH, Carlson JA et al (2005) Autonomous velocity and density profiler: EM-APEX. In: Proceedings of the IEEE/OES eighth working conference on current measurement technology, 2005. IEEE, pp 152–156

Sanford TB, Price JF, Girton JB, Webb DC (2007) Highly resolved observations and simulations of the ocean response to a hurricane. Geophys Res Lett. doi:10.1029/2007GL029679

Sanford TB, Price JF, Girton JB et al (2011) Upper-ocean response to Hurricane Frances (2004) observed by profiling EM-APEX floats[*]. J Phys Oceanogr 41:1041–1056. doi:10.1175/2010JPO4313.1

Sarafian E, Evans RL, Collins JA et al (2015) The electrical structure of the central Pacific upper mantle constrained by the NoMelt experiment. Geochem Geophys Geosyst 16:1115–1132. doi:10.1002/2014GC005709

Satake K, Fujii Y, Harada T, Namegaya Y (2013) Time and space distribution of coseismic slip of the 2011 Tohoku earthquake as inferred from tsunami waveform data. Bull Seismol Soc Am 103:1473–1492. doi:10.1785/0120120122

Saynisch J, Petereit J, Irrgang C et al (2016) Impact of climate variability on the tidal oceanic magnetic signal-A model-based sensitivity study. J Geophys Res Oceans 121:5931–5941. doi:10.1002/2016JC012027

Schnepf NR, Manoj C, Kuvshinov A et al (2014) Tidal signals in ocean-bottom magnetic measurements of the northwestern Pacific: observation versus prediction. Geophys J Int 198:1096–1110. doi:10.1093/gji/ggu190

Schnepf NR, Kuvshinov A, Sabaka T (2015) Can we probe the conductivity of the lithosphere and upper mantle using satellite tidal magnetic signals? Geophys Res Lett 42:3233–3239. doi:10.1002/2015GL063540

Schnepf NR, Manoj C, An C et al (2016) Time-frequency characteristics of tsunami magnetic signals from four Pacific Ocean events. Pure appl Geophys 173:3935–3953. doi:10.1007/s00024-016-1345-5

Segawa J, Toh H (1992) Detecting fluid circulation by electric field variations at the Nankai Trough. Earth Planet Sci Lett 109:469–476. doi:10.1016/0012-821X(92)90107-7

Shimizu H, Utada H (2015) Motional magnetotellurics by long oceanic waves. Geophys J Int 201:390–405. doi:10.1093/gji/ggv030

Shimizu H, Koyama T, Baba K et al (2010) Revised 1-D mantle electrical conductivity structure beneath the north Pacific. Geophys J Int 180:1030–1048. doi:10.1111/j.1365-246X.2009.04466.x

Singer BS (1995) Method for solution of Maxwell's equations in non-uniform media. Geophys J Int 120:590–598. doi:10.1111/j.1365-246X.1995.tb01841.x

Sladen A, Hébert H (2008) On the use of satellite altimetry to infer the earthquake rupture characteristics: application to the 2004 Sumatra event. Geophys J Int 172:707–714. doi:10.1111/j.1365-246X.2007.03669.x

Smith JT (1996a) Conservative modeling of 3-D electromagnetic fields, Part I: properties and error analysis. Geophysics 61:1308–1318. doi:10.1190/1.1444054

Smith JT (1996b) Conservative modeling of 3-D electromagnetic fields, Part II: biconjugate gradient solution and an accelerator. Geophysics 61:1319–1324. doi:10.1190/1.1444055

Stephenson D, Bryan K (1992) Large-scale electric and magnetic fields generated by the oceans. J Geophys Res 97:15467. doi:10.1029/92JC01400

Stommel H (1948) The theory of the electric field induced in deep ocean currents. J Mar Res 7:386–392

Stouffer RJ, Yin J, Gregory JM et al (2006) Investigating the causes of the response of the thermohaline circulation to past and future climate changes. J Clim 19:1365–1387. doi:10.1175/JCLI3689.1

Suetsugu D, Shiobara H, Sugioka H et al (2012) TIARES project—tomographic investigation by seafloor array experiment for the society hotspot. Earth Planets Sp 64:i–iv. doi:10.5047/eps.2011.11.002

Sugioka H, Hamano Y, Baba K et al (2014) Tsunami: ocean dynamo generator. Sci Rep 4:3596. doi:10.1038/srep03596

Szuts ZB (2012) Using motionally-induced electric signals to indirectly measure ocean velocity: instrumental and theoretical developments. Prog Oceanogr 96:108–127. doi:10.1016/j.pocean.2011.11.014

Taguchi E, Stammer D, Zahel W (2014) Inferring deep ocean tidal energy dissipation from the global high-resolution data-assimilative HAMTIDE model. J Geophys Res Oceans 119:4573–4592. doi:10.1002/2013JC009766

Tatehata H, Ichihara H, Hamano Y (2015) Tsunami-induced magnetic fields detected at Chichijima Island before the arrival of the 2011 Tohoku earthquake tsunami. Earth, Planets Sp 67:185. doi:10.1186/s40623-015-0347-3

Terker SR, Sanford TB, Dunlap JH, Girton JB (2013) The EM-POGO: a simple, absolute velocity profiler. Deep Sea Res Part II Top Stud Oceanogr 85:220–227. doi:10.1016/j.dsr2.2012.07.026

Thomson DJ, Lanzerotti LJ, Maclennan CG, Medford LV (1995) Ocean cable measurements of the tsunami signal from the 1992 Cape Mendocino earthquake. Pure Appl Geophys PAGEOPH 144:427–440. doi:10.1007/BF00874376

Toh H, Goto T, Hamano Y (1998) A new seafloor electromagnetic station with an Overhauser magnetometer, a magnetotelluric variograph and an acoustic telemetry modem. Earth Planets Sp 50:895–903. doi:10.1186/BF03352185

Toh H, Hamano Y, Ichiki M (2006) Long-term seafloor geomagnetic station in the northwest Pacific: a possible candidate for a seafloor geomagnetic observatory. Earth Planets Sp 58:697–705. doi:10.1186/BF03351970

Toh H, Satake K, Hamano Y et al (2011) Tsunami signals from the 2006 and 2007 Kuril earthquakes detected at a seafloor geomagnetic observatory. J Geophys Res 116:B02104. doi:10.1029/2010JB007873

Tsugawa T, Saito A, Otsuka Y et al (2011) Ionospheric disturbances detected by GPS total electron content observation after the 2011 off the Pacific coast of Tohoku Earthquake. Earth Planets Sp 63:875–879. doi:10.5047/eps.2011.06.035

Tyler RH (2005) A simple formula for estimating the magnetic fields generated by tsunami flow. Geophys Res Lett 32:L09608. doi:10.1029/2005GL022429

Tyler R (2015) Electromagnetic coupling of ocean flow with the earth system. Terr Atmos Ocean Sci 26:41–52. doi:10.3319/TAO.2014.08.19.04(GRT)

Tyler RH, Mysak LA (1995) Motionally-induced electromagnetic fields generated by idealized ocean currents. Geophys Astrophys Fluid Dyn 80:167–204. doi:10.1080/03091929508228954

Tyler RH, Mysak LA, Oberhuber JM (1997) Electromagnetic fields generated by a three dimensional global ocean circulation. J Geophys Res Oceans 102:5531–5551. doi:10.1029/96JC03545

Tyler RH, Maus S, Lühr H (2003) Satellite observations of magnetic fields due to ocean tidal flow. Science 299(5604):239–241. doi:10.1126/science.1078074

Utada H, Shimizu H, Ogawa T et al (2011) Geomagnetic field changes in response to the 2011 off the Pacific Coast of Tohoku Earthquake and Tsunami. Earth Planet Sci Lett 311:11–27. doi:10.1016/j.epsl.2011.09.036

Vivier F, Maier-Reimer E, Tyler RH (2004) Simulations of magnetic fields generated by the Antarctic Circumpolar Current at satellite altitude: can geomagnetic measurements be used to monitor the flow? Geophys Res Lett. doi:10.1029/2004GL019804

Von Arx WS (1950) Electromagnetic method for measuring the velocities of ocean currents from a ship under way. Massachusetts Institute of Technology and Woods Hole Oceanographic Institution, Cambridge

Wang B, Guo X, Liu H, Gong C (2015). On the magnetic anomaly at Easter Island during the 2010 Chile tsunami. Theor Appl Mech Lett 5(5):187–190

Weaver JT (1965) Magnetic variations associated with ocean waves and swell. J Geophys Res 70:1921–1929. doi:10.1029/JZ070i008p01921

White A (1979) A sea floor magnetometer for the continental shelf. Mar Geophys Res 4:105–114. doi:10.1007/BF00286148

Wollaston C (1881) Discussion of the paper by AJS Adams "earth Currents" (2nd paper). J Soc Telegr Eng Electr 10:50–51

Young FB, Gerrard H, Jevons W (1920) On electrical disturbances due to tides and waves. Philos Mag Ser 6(40):149–159. doi:10.1080/14786440708636105

Zhang L, Baba K, Liang P et al (2014a) The 2011 Tohoku Tsunami observed by an array of ocean bottom electromagnetometers. Geophys Res Lett 41:4937–4944. doi:10.1002/2014GL060850

Zhang L, Utada H, Shimizu H et al (2014b) Three-dimensional simulation of the electromagnetic fields induced by the 2011 Tohoku tsunami. J Geophys Res Solid Earth 119:150–168. doi:10.1002/2013JB010264